ACS OMEGA

http://pubs.acs.org/journal/acsodf

Article

Development of Density-Functional Tight-Binding Parameters for the Molecular Dynamics Simulation of Zirconia, Yttria, and Yttria-Stabilized Zirconia

Aulia Sukma Hutama,* Lala Adetia Marlina, Chien-Pin Chou, Stephan Irle, and Thomas S. Hofer

Cite This: *ACS Omega* 2021, 6, 20530−20548

Read Online

ACCESS | Metrics & More | Article Recommendations | Supporting Information

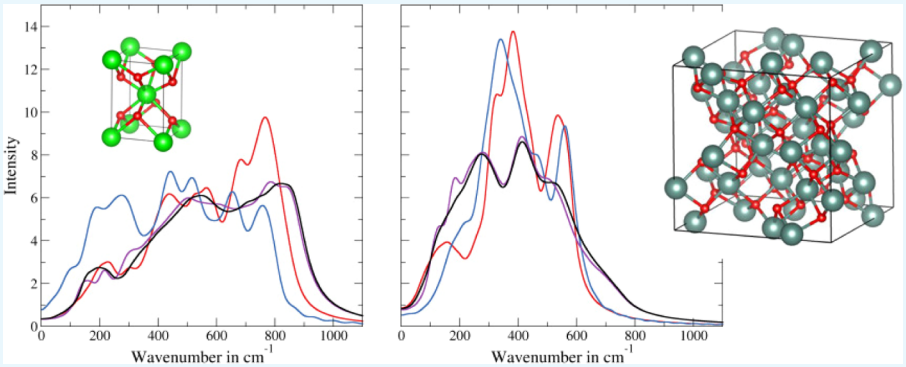

ABSTRACT: In this work, a set of density-functional tight-binding (DFTB) parameters for the Zr−Zr, Zr−O, Y−Y, Y−O, and Zr−Y interactions was developed for bulk and surface simulations of ZrO_2 (zirconia), Y_2O_3 (yttria), and yttria-stabilized zirconia (YSZ) materials. The parameterization lays the ground work for realistic simulations of zirconia-, yttria-, and YSZ-based electrolytes in solid oxide fuel cells and YSZ-based catalysts on long timescales and relevant size scales. The parameterization was validated for the zirconia and yttria polymorphs observed under standard conditions based on density functional theory calculations and experimental data. Additionally, we performed DFTB-based molecular dynamics (MD) simulations to compute structural and vibrational properties of these materials. The results show that the parameters can give a qualitatively correct phase ordering of zirconia, where the tetragonal phase is more stable than the cubic phase at a lower temperature. The lattice parameters are only slightly overestimated by 0.05−0.1 Å (2% error), still within the typical accuracy of first-principles methods. Additionally, the MD results confirm that zirconia and yttria phases are stable against transformations under standard conditions. The parameterization also predicts that vibrational spectra are within the range of 100−1000 cm^{-1} for zirconia and 100−800 cm^{-1} for yttria, which is in good agreement with predictions both from full quantum mechanics and a recently developed classical force field. To further demonstrate the advantage of the developed DFTB parameters in terms of computational resources, we conducted DFTB/MD simulations of the YSZ4 and YS12 models containing approximately 750 atoms.

1. INTRODUCTION

Zirconia (ZrO_2) is one of the most important oxide materials with a wide range of applications. Due to its excellent mechanical strength, the bulk phase is commonly used for refractory and structural materials,[1] while surface applications such as support materials for various catalytic processes are growing rapidly.[2−5] The phase stability of pure ZrO_2 at standard atmospheric pressure (1.013 bar) is widely known. The monoclinic phase (space group $P2_1/c$) is the most stable phase at room temperature up to 1478 K, followed by the tetragonal phase (space group $P4_2/nmc$), which is stable from 1478 to 2650 K, and the cubic phase (space group $Fm\bar{3}m$) is the high-temperature phase up to its melting point of 2983 K.[6]

Zirconia doped with other aliovalent metals such as Mg, Ca, or Y is utilized mainly in electrolytes in solid oxide fuel cells (SOFCs) due to its high ionic mobility at elevated temperature.[7−11] Doping of metals with different valences creates oxygen vacancy sites. Oxygen (or oxide) centers will be able to migrate through the vacant sites from the cathode to the anode and in this way create an electric current. Among the metal-doped zirconia-based materials, yttria-stabilized zirconia (YSZ) remains most popular. Due to its availability, chemical stability, non-toxicity, low cost, and good ionic conductivity, YSZ is

Received: May 17, 2021
Accepted: July 15, 2021
Published: July 31, 2021

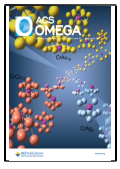

frequently employed not only as an electrolyte in SOFCs but also as an oxygen sensor[12,13] and catalyst or catalyst support.[14]

In order to enhance the performance of YSZ-based SOFCs and catalysts, an atomic-level understanding of structural, dynamical, and thermodynamic properties on experimentally relevant length and timescales is necessary. While being often difficult to obtain experimentally, useful insights into these processes can be obtained from computer simulations. When choosing a method for computer simulations, one usually aims to maintain a reasonable balance between computational effort and simulation accuracy. Computationally economical simulation methods often rely on empirical or fitted interatomic potentials, such as classical molecular mechanics (MM) and the ReaxFF method.[15−32] A drawback of the MM methods is that the electron−electron interaction is not explicitly included in the simulation, and therefore, some properties such as bond breaking or/and effects of external electric fields on the systems cannot be elucidated using this approach. We note that the ReaxFF method is based on a bond order formalism to enable the description of the bond breaking processes; however, charge transfer processes, for example, occurring in oxygen vacancy migration, are insufficiently described. On the other hand, electronic structure methods that can explicitly account for electron−electron interactions, most notably density functional theory (DFT), have become the standard workhorse in computational materials science. However, due to the associated high computational costs, in particular related to memory, the treatable number of atoms is strongly limited compared to that in force field approaches.

A recently emerging method called as the self-consistent-charge density-functional tight-binding (SCC-DFTB), also known as the second-order DFTB (DFTB2) method,[33,34] bridges the gap between these classical approaches and electronic structure theory. This semiempirical methodology enables longer simulation periods and larger, more adequate model systems in molecular dynamics (MD) studies of nanoscale clusters, thereby still retaining the quantum mechanical (QM) treatment of electron−electron interactions. DFTB2 is approximately three orders of magnitude faster than DFT with ideally comparable accuracy. With further extensions to the DFTB2 method, such as the spin-polarized scheme[35,36] and time-dependent formalisms,[37,38] this method has become a versatile tool for investigations in chemistry and materials science. DFTB2 has been used to investigate many applications in materials science such as simulations of oxygen vacancies in titania,[39] graphene formation on metal substrates,[40] and, recently, H_2O and NH_3 absorption on titania *via* a DFTB/MM extension.[41]

Certainly, CP2K and other linear scaling DFT codes are nowadays able to perform "heroic" calculations on long timescales for large systems. However, we would like to point out that the computational resources needed for such calculations are not necessarily accessible to the broader community, and thus, systematic studies probing many degrees of freedom (temperature, oxygen vacancy density, impurities, *etc.*) at the DFT level are still beyond reach for the majority of researchers, and DFTB provides a feasible alternative in such cases.

In order to extend the applicability of the DFTB2 method to describe solid states and surfaces of Zr-based oxides, we report here the development of DFTB2 parameters for Y−Zr−O pair interactions. These parameters are a key prerequisite for performing MD simulations on model zirconia systems with realistic length scales and long timescales. The new DFTB2 parameters were optimized and validated with respect to geometric data with the associated energetic performance calibration based on different ZrO_2 and Y_2O_3 polymorphs observed at the standard atmospheric pressure (1.013 bar).

2. METHODS

2.1. Brief Overview of the DFTB2 Method. The detailed definition and derivation of the DFTB2 method have been described in the original paper[33,34] and have been the subject of in-depth review articles.[42,43] Here, we provide a brief summary to emphasize the focal point that is utilized in this paper.

DFTB2 takes the approximation of the total Kohn−Sham DFT energy using the density fluctuation $\delta\rho(r)$ around the reference density $\rho_0(r)$ *via* a Taylor expansion. In this way, the total energy can be expressed as summation of three terms, namely, the band structure energy, E_{band}, the repulsive energy E_{rep}, and a SCC contribution, E_{SCC}

$$E^{DFTB2} = E_{band} + E_{rep} + E_{SCC} = \sum_{i}^{occ} n_i \epsilon_i + E_{rep} + E_{SCC} \tag{1}$$

From eq 1, the first term, the band structure energy, E_{band}, is the summation of the orbital energies ϵ_i over all occupied orbitals Ψ_i. The second term, E_{rep}, accounts for the core−core interactions, contributions arising from the exchange−correlation energy, and other contributions in the form of a set of distance-dependent pairwise terms $V_{\alpha\beta}^{repulsive}$ with $R_{\alpha\beta}$ being the associated pair distance

$$E_{rep} = \frac{1}{2} V_{\alpha\beta}^{rep}(R_{\alpha\beta}) \tag{2}$$

The final term (E_{SCC}) can be explained as the contributions arising from charge−charge interactions in the system. The band structure and SCC energies are often considered as the electronic energy.

The orbitals Ψ_i are constructed in the form of a linear combination of atomic orbitals (LCAO)

$$\Psi_i(r) = \sum_{\mu} \sum_{\mu \in \alpha} \phi_\mu c_{i\mu}(r - R_\alpha) \tag{3}$$

Thereby, using a minimal basis set, that is, only valence electrons are considered, similar as in standard tight-binding theory. The (pseudo)atomic orbitals are determined by self-consistently solving Kohn−Sham-like equations, usually using an LDA or GGA exchange−correlation functional

$$\left[-\frac{1}{2}\nabla^2 + V_{ne}(r) + \int \frac{\rho_0(r')}{|r - r'|} dr' + V_{XC}(r) + V_{conf}(r)\right] \phi_\mu(r) = \epsilon_\mu \phi_\mu(r) \tag{4}$$

These Kohn−Sham-like equations (eq 4) contain additional terms being the so-called confining potentials, $V_{conf}(r)$, in order to mimic the bonding environment in molecules or solids. Several approaches for the confining potential have been proposed in the literature. The traditional DFTB confining potential usually has the form of a harmonic potential[34]

$$V_{conf}(r) = (r/r_0)^2 \tag{5}$$

https://doi.org/10.1021/acsomega.1c02411
ACS Omega 2021, 6, 20530−20548

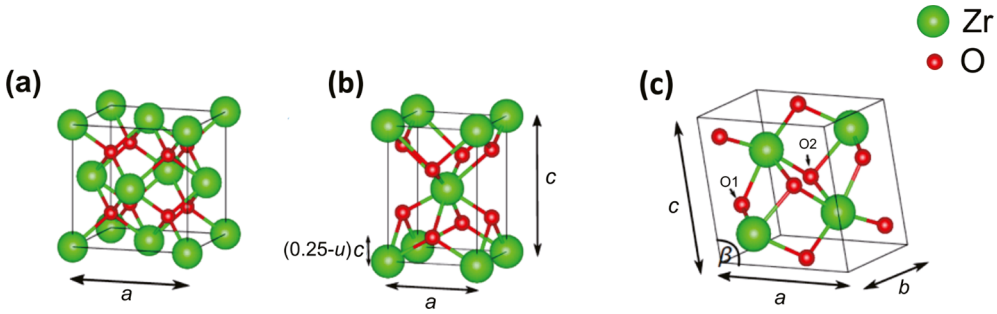

Figure 1. Phases of zirconia considered at the standard atmospheric pressure (1.013 bar): (a) cubic, (b) tetragonal, and (c) monoclinic.

with the value of r_0 being usually optimized in order to achieve good agreement in the respective band structure. Typically, the values for r_0 are 1.5−2 times the atomic covalent radius.

The most recent approach for the confining potential takes the form of the Woods−Saxon potential given as

$$V_{\text{conf}}(r) = \frac{W}{1 + \exp(-a(r - r_0))} \tag{6}$$

with the parameters W, a, and r_0 determining the shape of the potential. W is the amplitude of the potential, a is proportional to the gradient of the slope at $r = r_0$, and r_0 is the position where $V_{\text{conf}}(r)$ is equal to one-half of W. In order for the Woods−Saxon confining potential to be effective, the Dirac−Kohn−Sham-like eigenvalue equation is used instead of the Kohn−Sham-like equation (eq 7), enabling also the inclusion of electronic relativistic effects[44]

$$\left[-ic\alpha\nabla + (\beta - 1)c^2 + V_{\text{ne}}(r) + \int \frac{\rho_0(r')}{|r - r'|}\,dr' + V_{\text{XC}}(r) + V_{\text{conf}}(r)\right]\phi_\mu(r) = \epsilon_\mu\phi_\mu(r) \tag{7}$$

with c being the velocity of light, α and β are Dirac matrices, and 1 stands for the unit matrix. $\phi_\mu(r)$ represents the spinor-like atomic radial wave functions with energy ϵ_μ, which include both scalar and spin−orbit relativistic effects. The pseudoatomic orbitals are then generated by averaging the total four components of $\phi_\mu(r)$. In our case, the relativistic effect for the metal will yield more accurate orbital energy and improve the band structure. Figure S1 shows an example of the Zr metal (hexagonal close-packed, HCP) band structure without the inclusion of the relativistic effect. Even the small variation of 4d orbital energy will induce compressed conduction bands if the relativistic effect is not included. Also, the low-lying conduction bands are considerably affected.

2.2. Parameterization Procedures and Computational Details. The electronic parameterizations for Zr and Y have been conducted in the previous studies employing the Woods−Saxon confining potential by taking the bulk Zr and Y band structures calculated at the PBE-PAW level of theory as refs 45 and 46 (see Table S1 displaying the Woods−Saxon orbital confining potential). The electronic parameterization considered valence electrons from 4d and 5s orbitals and the empty 5p orbital for the metal atoms. The explicit valence electrons were considered to give an adequate description of the low-lying valence and conduction bands while keeping the computational cost to the minimum. The confining potential for orbitals and the density of O and the associated O−O repulsive pair potential were taken from the mio-1-1 set.[34] In the current approach, the Zr−O, O−Zr, Y−O, and O−Y Hamiltonian and overlap integrals were obtained by the integration of the pseudoatomic orbitals obtained from the Dirac−Kohn−Sham equation in eq 7 for Y and Zr and the O atomic orbitals from the mio-1-1 set based on the density superposition scheme.

Inspired by the idea of Hellström *et al.*,[47] the repulsive potential for Zr−O was fitted to different phases of zirconia. Hellström *et al.*[47] discovered that the correct energetics of various bulk ZnO polymorphs can be produced by reparameterizing the Zn−O repulsive potential from the published znorg set[48] by including different polymorphs with different coordination numbers into the training set. In this study, the Zr−O potential was fitted to two phases, namely, the cubic (c-ZrO_2) and tetragonal (t-ZrO_2) phases (Figure 1a,b), despite both structures having similar Zr and O coordination numbers, being 8 and 4 for Zr and O, respectively. However, the difference is that the tetragonal phase is rather more complex than the cubic phase since its unit cell is characterized by three distinct structural parameters: the lattice parameters a and c and the internal parameter u, which measures the distortion from the ideal oxygen position occupying the 4d site in the z direction (in fractional coordinates) from the cubic phase; the ideal cubic phase has a value of z of 0.25 (*i.e.*, $u = 0.25 - z$). The cubic phase on the other hand is only characterized by a single structural parameter, that is, the lattice parameter a. The structural characteristics imply that the cubic phase has only one distinct Zr−O bond, while the tetragonal phase has two. The unit cell of the monoclinic phase (m-ZrO_2, Figure 1c) is characterized by 13 distinct structural parameters: the lattice parameters a, b, and c; the angle between the lattice parameters a and c, namely, γ; and three distinct positions (x, y, z) of Zr, O1, and O2 occupying the 4e site. The monoclinic phase has six distinct Zr−O bonds, and its structure is the most complicated among the phases observed at 1.013 bar. The fitting of DFTB repulsive potentials to phases with many different bond lengths is quite unfavorable because it may cause oscillation in the potential.[49]

The Y−O repulsive pair potential was constructed by fitting to the cubic Y_2O_3 phase (c-Y_2O_3, space group $Ia\bar{3}$). The Y_2O_3 cubic structure, as shown in Figure 2, is a distorted cubic fluorite structure. In the unit cell, 8 and 24 Y atoms occupy the b and d sites, respectively, while 48 O atoms occupy the e site; thus, the total number of atoms in the unit cell is 80 (16 Y_2O_3 units). In such a case, fitting to many bond lengths is inevitable. Nevertheless, the obtained parameters can describe the properties of the bulk phases in reasonable agreement within DFTB accuracy.

https://doi.org/10.1021/acsomega.1c02411
ACS Omega 2021, 6, 20530−20548

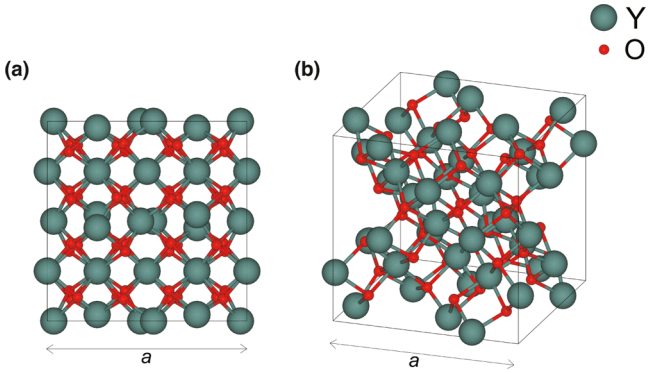

Figure 2. (a) Orthographic and (b) oblique projections of the cubic phase of yttria (c-Y_2O_3).

Previous work reports that at high temperature and an ambient pressure of 1.013 bar, the hexagonal phase of Y_2O_3 is the most stable one.[50] However, a cubic−hexagonal phase transition occurs near the melting point of Y_2O_3 above 2500 K. The hexagonal phase of Y_2O_3 appears to gain less attention from experiments due to the high-temperature nature of the phase. Therefore, the Y−Y and Y−O parameters are only validated against the cubic form c-Y_2O_3.

In the present work, we focused on the accuracy of the metal−oxygen repulsive potentials. The cutoff radius of the Zr−Zr pair was set so that the value did not interfere with the Zr−O repulsive parameterization while maintaining a reasonable geometry of the experimental Zr bulk phase.[46] However, such an approach did not seem to work for the case of the Y−O parameterization, as the Y−Y repulsive potential cutoff value will eventually affect the Y−O repulsive pair due to the complexity of the Y_2O_3 structure. Because of this, we carefully adjusted both Y−Y and Y−O repulsive pair cutoff radii to give a correct description of the geometrical and structural properties. The Zr−Y repulsive potential was made similar to that of the Zr−Zr pair since in YSZ, the Zr−Y distance is close to the Zr−Zr distance. The Zr−Zr and Y−Y repulsive pairs were fitted to the room temperature HCP phase (space group $P6_3/mmc$) of the pristine metal.

The DFT reference data were obtained by scanning reference phases from approximately 70−130% volume of the DFT equilibrium geometry with intervals of approximately 5% of the volume. The repulsive potential was obtained by fitting the difference between the DFT and DFTB energies as a function of the pair distance presented in Figure S2. We used the purely repulsive potential since the contribution from the DFTB electronic energy as a function of distance (E_{elec}) increases monotonically, as presented in Figure S2. Therefore, in order to obtain the correct potential energy curve, the purely repulsive energy term must be employed. The energy differences were then divided by the coordination number and then fitted using a polynomial function. Polynomial fitting with a degree of at least 2 was employed to ensure the smoothness of the potential and the continuity of the potential's first derivative. The repulsive potential cutoff radii for all pairs created in the present work are shown in Table 1. The repulsive cutoff radii for Zr−O and Y−O pairs are relatively short, but they are sufficiently long to cover all occurring Zr−O and Y−O distances in the respective training sets.

The DFT reference calculations were performed employing the PBE functional[51] within a PAW[52] basis as implemented in the VASP code version 5.2.[53−56] The explicit valence electron configurations are $4s^24p^65s^24d^2$ for Zr, $4s^24p^65s^24d^1$ for Y, and $2s^22p^4$ for O. The kinetic energy cutoff was set to 550 eV. The k-point sampling grid in the first Brillouin zone was based on the Monkhorst−Pack scheme. In the case of all zirconia phases, a 16 × 16 × 16 grid was applied, while a 2 × 2 × 2 grid proved sufficient for yttria and YSZ. All DFTB calculations were performed using the DFTB+[43,57] code version 19.1 with the same number of k-points as in the DFT reference calculations. Phonon calculations were carried out using the phonopy code version 2.9.3[58] interfaced with the DFTB+ calculator.

Table 1. Repulsive Cutoff Radii for the Individual Pair Interactions

pair	reference system	cutoff radius (Å)
Zr−Zr	HCP	3.30
Y−Y	HCP	3.65
Zr−O	cubic, tetragonal	2.50
Y−O	cubic	2.50

The pseudoatomic orbitals, density, and potential for Zr and Y were obtained using the relativistic one-center atomic code (ONECENT).[44] The Zr−Zr, Zr−O, O−Zr, Y−O, O−Y, Y−Y, Zr−Y, and Y−Zr Hamiltonian and overlap matrix elements were then computed using the two-center integral code (TWOCENT)[59] interfaced to the automatic DFTB parameterization toolkit.[60,61] The polynomial fitting and the conversion to the standard 3rd−5th-order spline format for the repulsive potentials were carried out using the code by Bodrog *et al.*[49] The respective SK files are available in the Supporting Information.

2.3. Parameter Validation. To further validate the generated DFTB parameters, MD simulations were conducted to determine the phase stability, radial distribution functions (RDFs), and vibrational properties of ZrO_2, Y_2O_3, and YSZ. Initially, the unit cells for ZrO_2 and Y_2O_3 were expanded to 4 × 4 × 4 and 2 × 2 × 2 supercells, yielding systems containing 768 and 640 atoms, respectively. However, we found negligible difference in the properties with the smaller 2 × 2 × 2 and 1 × 1 × 1 unit cell expansion with 96 and 80 atoms for ZrO_2 and Y_2O_3, respectively. Therefore, further MD analyses for ZrO_2 and Y_2O_3 were conducted based on the smaller expansion of the unit cell.

The initial systems for YSZ have been constructed from the 4 × 4 × 4 expansion of the ZrO_2 unit cell (768 atoms) by randomly replacing zirconium with yttrium and deleting one randomly selected oxygen per two cationic substitutions. To uphold an integer stoichiometry of the simulation system, the cationic substitution has to be carried out in increments of two. The various YSZ-systems considered in this study are summarized in Table 2.

All MD simulations have been performed using a time step of 2.0 fs to integrate the equations of motion using the

Table 2. YSZ Systems with Different Yttria Contents $c_{Y_2O_3}$ in mol % and the Respective Number of Ions Considered in this Study

model	$c_{Y_2O_3}$	N_{Zr}	N_Y	N_O	N_{tot}
YSZ4	4.06	236	20	502	758
YSZ12	11.79	202	54	485	741

https://doi.org/10.1021/acsomega.1c02411
ACS Omega 2021, 6, 20530−20548

velocity−Verlet algorithm. To achieve thermal and pressure control along the simulation (*i.e.*, an *NPT* ensemble), the Berendsen weak coupling thermostat and manostat algorithms[62] were employed, with the associated relaxation times τ_T and τ_P being set to 0.1 and 1.0 ps, respectively.

To characterize dynamical properties, vibrational power spectra have been evaluated *via* Fourier transform (FT) of the associated velocity autocorrelation function $C(t)$, given as

$$C(t) = \frac{\langle \mathbf{v}_0 \mathbf{v}_t \rangle}{\langle \mathbf{v}_0 \mathbf{v}_0 \rangle} \quad (8)$$

with $\mathbf{v}_0$ and $\mathbf{v}_t$ representing the velocity vector of the entire system at a time origin and time t, respectively. In this study, dedicated simulation trajectories employing a tight spacing of configurations of 1 MD step (2 fs) was employed. A correlation window of 500 MD steps corresponding to a 1 ps time interval was employed in all cases, thereby considering the velocities of all atoms in the analyzed systems. An exponential window with a decay constant of 4 ps^{-1} was applied in the subsequent FT. In the case of the large systems (768 and 640 atoms for *t*-ZrO_2 and *c*-Y_2O_3, respectively), a sampling period of 3000 MD steps (6 ps) after a 1 ps equilibration period was employed to determine the vibrational spectra, whereas for the smaller systems, the sampling period could be enlarged to 20000 MD steps (40 ps) in the case of *t*-ZrO_2 (96 atoms) and *c*-Y_2O_3 (80 atoms).

In order to assess the performance of the DFTB parameterizations, all-QM MD simulations of the latter systems have been performed at the PBEsol[63] level of theory using Crystal17[64] to carry out the evaluation of energy and forces. After 1000 steps (2 ps) of equilibration, the systems have been sampled for another 2000 MD steps corresponding to a sampling period of 4 ps.

3. RESULTS

3.1. Electronic Band Structures. The Woods−Saxon confining potentials, orbital energies, and Hubbard parameters for Zr and Y were taken from previous studies and without modification.[45,46] These electronic parameters are found to closely mimic those of the PBE valence and conduction band structures up to 5 eV above the Fermi level for the HCP crystal structure, as shown in Figure S3. The band structures determined at the DFTB2 level show good qualitative agreement with reference PBE-PAW calculations for the metal oxides for both the valence bands and several low-lying conduction bands. The predicted DFTB2 band gap energies for *m*-ZrO_2, *t*-ZrO_2, *c*-ZrO_2, and *c*-Y_2O_3 are obtained as 4.3, 4.3, 3.7, and 4.6 eV, respectively. The corresponding values from the reference PBE-PAW calculations are 3.6, 3.8, 3.3, and 4.1 eV for *m*-ZrO_2, *t*-ZrO_2, *c*-ZrO_2, and *c*-Y_2O_3, respectively. Both levels of theory predict lower band gaps than the experimental values of 5.4−5.8 eV for ZrO_2 polymorphs[65,66] and 5.6−5.8 eV for *c*-Y_2O_3,[67] although the DFTB2 band gaps are slightly larger than those obtained in the PBE-PAW case. The underestimation of the band gap is not surprising since it is a known shortcoming in DFT-based methods, arising from the self-interaction error. The underestimation of the band gap can be remedied for instance by inclusion of onsite correction terms to the DFTB Hamiltonian, the so-called DFTB + U[68] method, without modifying the electronic parameters. Another way to remedy the DFTB self-interaction error is by splitting the exchange operator into the short- and long-range parts, that is, range-separated DFTB.[69,70] However, to the best of our knowledge, range-separated DFTB has not been tested for solid-state systems, for which the PBE functional is typically preferable over functionals with hybrid exchange. Nevertheless, the present work demonstrates the good transferability of the employed electronic parameters to different crystal structures.

3.2. Properties of the Bulk Phases. *3.2.1. Zr and Y Metal.* Both Zr and Y crystallize in the HCP structure at room temperature. In the present study, we only focus on the geometry of the bulk phase of the metals. Table 3 shows the results of the lattice parameters of the HCP phase calculated at PBE-PAW and DFTB2 levels of theory in comparison with the available experimental data and previously reported DFT calculations. It is shown that the *a* lattice parameter of both metals is shorter by around 0.03−0.09 Å compared to PBE-PAW and experimental values. On the other hand, the *c* lattice parameter is longer by 0.06−0.09 Å compared to DFT and experimental values; thus, the *c*/*a* ratio is close to the ideal *c*/*a* ratio of 1.633, where the M−M bond length values are equal in the structures. The DFTB parameters seem to favor the equal bond length in the system. Although further refinement of these parameters is plausible, the deviation of the lattice parameter is below 2%; thus, the comparison between DFT and experimental values is acceptable. Therefore, we employ these Zr−Zr and Y−Y repulsive potentials for further parameter development.

Table 3. Lattice Parameters of the HCP Phase of Bulk Zr and Y

metal	lattice parameter (Å)	DFTB2	PBE-PAW	experiment
Zr	*a*	3.205	3.235[a], 3.240[115]	3.233[116]
	c	5.239	5.163[a], 5.178[115]	5.146[116]
Y	*a*	3.559	3.654[a]	3.647[117]
	c	5.764	5.664[a]	5.731[117]

[a]Present study.

3.2.2. ZrO_2. Table 4 lists the lattice parameters of the three considered zirconia phases compared to current DFT calculations, experimental values, and previously reported theoretical results. In general, the DFTB2 parameter set is able to reproduce the cubic phase lattice parameter in good agreement with DFT and experimental reference data. Due to the instability of pure cubic zirconia at lower temperature, the experimental value of the cubic lattice parameter was taken from the extrapolation to room temperature. For the tetragonal phase, the lattice parameters are in good agreement with DFT and experimental values. The computed value for the lattice parameter *a* is shorter by about 0.05 Å compared to the newly calculated DFT results and experimental data. Meanwhile, the lattice parameter *c* calculated using DFTB2 is shorter by 0.01 Å compared to the new DFT data. Similarly, the computed DFTB2 *u* value is also in good agreement with the present DFT reference and the experimental reference. For the monoclinic phase, the DFTB2 results show that the lattice parameters *a* and *b* are shorter by approximately 0.13 Å, while *c* is shorter by approximately 0.07 Å compared to the DFT case and experimental values. As a consequence, the volume is smaller than the DFT value, and the Zr−O bonds are shorter. However, it should be noted that albeit the monoclinic phase is the most stable phase at room temperature, it has the most complicated structure among the other phases observed at

https://doi.org/10.1021/acsomega.1c02411
ACS Omega 2021, 6, 20530−20548

Table 4. Selected Bulk Properties of Zirconia Obtained from DFT, DFTB2, and Experiment[a]

phase	parameter	DFTB2	PBE-PAW	experiment
cubic	a (Å)	5.111	5.118[b], 5.145[77]	5.114[c]
	E_{form}/ZrO_2 (eV)	0.36	0.212[b], 0.199[77]	N/A
	B_0 (GPa)	231	235[b]	N/A
tetragonal	a (Å)	3.598	3.624[b], 3.642[77]	3.64[83]
	c (Å)	5.260	5.272[b], 5.295[77]	5.27[83]
	u	0.065	0.057[b], 0.054[77]	0.065[83]
	E_{form}/ZrO_2 (eV)	−0.16	0.110[b], 0.109[77]	0.062−0.08[d]
	B_0 (GPa)	388	152[b]	N/A
monoclinic	a (Å)	5.093	5.192[b], 5.21[77]	5.169[118]
	b (Å)	5.096	5.246[b], 5.286[77]	5.232[118]
	c (Å)	5.422	5.377[b], 5.388[77]	5.341[118]
	β (°)	99.13	99.6[b], 99.6[77]	99.3[118]
	E_{form}/ZrO_2 (eV)	0.00	0.00	0.00
	B_0 (GPa)	240	132.18[b]	95−149[119,120]

[a] E_{form} is defined as $E_{t,c} - E_m$. [b] Present study. [c] Extrapolated to room temperature from ref 121. [d] $m - t$ phase transformation enthalpy taken from refs 122−124.

1.013 bar. At equilibrium geometry, the first nearest neighbor Zr−O bond in the cubic phase has the same distance of 2.22 Å, and the tetragonal phase has two Zr−O distinct bond lengths at 2.08 and 2.44 Å, while in the monoclinic phase, six distinct Zr−O nearest neighbor distances ranging from 2.06 to 2.29 Å are observed. It is possible that the contributions of different Zr−O bonds in the monoclinic phase are only approximately described by our repulsive potential since the fitting systems have different coordination numbers from those occurring in the monoclinic phase. Nevertheless, the geometry of the monoclinic phase calculated using the new parameters is still within the accuracy range of the DFTB2 method.

The Mulliken charges of Zr and O of the optimized geometries are tabulated in Table S2. The average Mulliken charges for Zr and O in ZrO_2 are *ca.* +1 and −0.5, respectively. In general, the magnitude of the Mulliken charges is much lower than that of the assumed formal oxidation state (FOS) of Zr and O, being +4 and −2, respectively. However, it should be noted that partial atomic charge analysis based on partitioning of the wave function does not correspond to the FOSs that are a popular concept in inorganic chemistry and strongly depends on the choice of the basis set. The underestimation of Mulliken charges with respect to FOSs is method-independent and also appears in DFT calculations. For example, the Mulliken charges on Ti and O in TiO_2 polymorphs are predicted to be *ca.* +0.65 and −0.32, respectively, at the PBE level, while the authors concluded that "Ti^{3+}" is a better description of Ti in TiO_2 than "Ti^{4+}" using Bader charge density analysis.[71] In the case of ZrO_2, earlier theoretical calculations also proposed that Zr is in the +2 oxidation state rather than the +4 state due to significant covalency of bonds in ZrO_2.[72,73] In addition, DFT calculations on ZrO_2 also predict that Zr has a Mulliken charge of +1.38, which is close to our computed value.[74] In conclusion, Mulliken charge analyses can be conducted to predict qualitatively the charges of the species in the material but is not to be related to FOSs.

The associated bulk moduli were obtained by fitting of the energy *versus* volume ($E-V$) curves in Figure 3 to the Birch−Murnaghan equation of state.[75] It is shown in Table 4 that the fitting to both the cubic and tetragonal phases yields a larger bulk modulus for the tetragonal phase by 230 GPa than the DFT results, while the bulk modulus of the cubic phase is 4 GPa lower compared to the DFT results. Since the cubic and tetragonal phases are high-temperature phases, experimental bulk moduli are not available. The reason for the observed overestimation is that more emphasis was directed toward the tetragonal phase during the parameterization process, so that it is more stable than the monoclinic phase. In any case, this overestimation of the bulk modulus has no impact on the properties of interest. For the monoclinic phase, the bulk moduli from the DFTB2 calculations show a similar trend as in the tetragonal case, where the values overestimate current DFT values. However, the present DFT bulk modulus is much lower compared to the previous PBE-PAW calculation but closer to the experimental value. The discrepancy between the bulk moduli obtained from DFTB2 and DFT might be caused by different Zr and O coordination numbers of m-ZrO_2 compared to the training set. A similar trend in the bulk modulus was also observed in DFTB2 calculations of the ZnO polymorphs by Hellström *et al.*, where different phases overestimate the bulk modulus up to 100 GPa.[47] This comparison provides insights into the transferability problems of DFTB2 parameters for

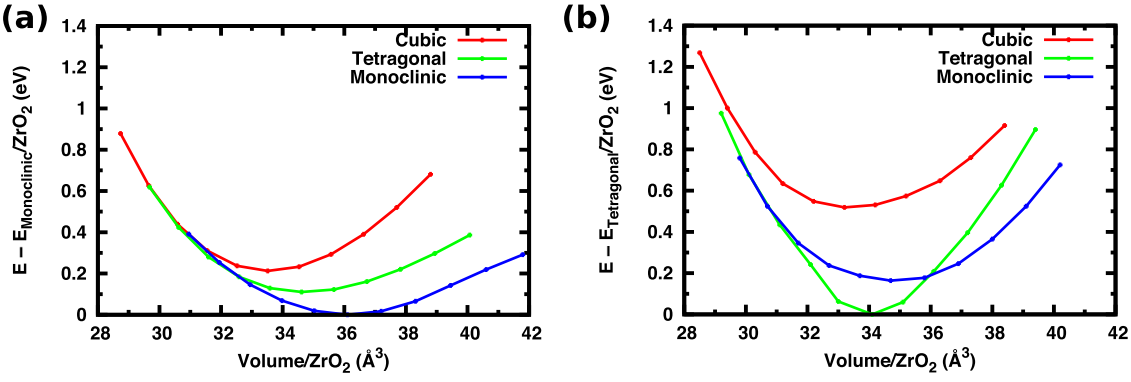

Figure 3. Relative energy *vs* volume per ZrO_2 unit for all phases of bulk zirconia obtained using (a) PBE-PAW and (b) DFTB2. The equilibrium energy of the most stable phase geometry was used as the energy reference for each level of theory.

https://doi.org/10.1021/acsomega.1c02411
ACS Omega 2021, 6, 20530−20548

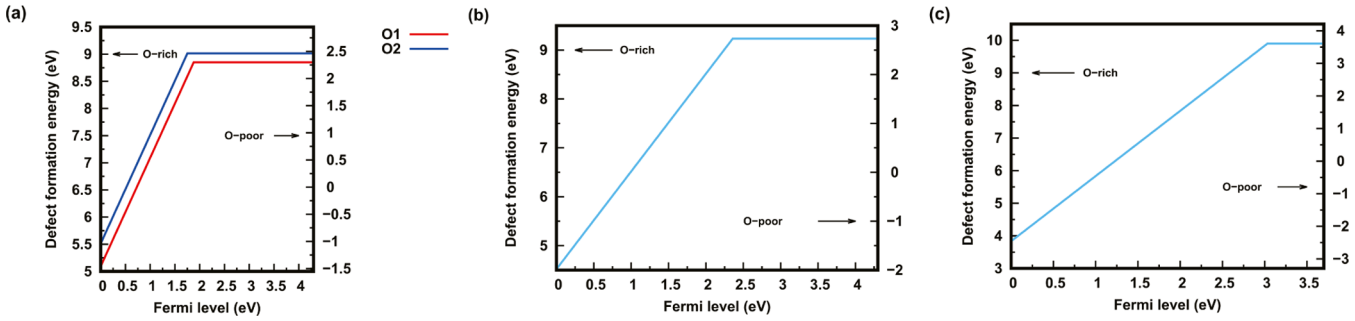

Figure 4. Defect formation energies of an oxygen vacancy in (a) m-ZrO_2, (b) t-ZrO_2, and (c) c-ZrO_2 plotted as a function of the Fermi level for oxygen-rich (left y-axis) and oxygen-poor (right y-axis) conditions. m-ZrO_2 has two different oxygen defect sites explained in Figure 1. Defect formation energies for c-ZrO_2 are calculated from the unrelaxed geometries.

complex solid-state systems, where geometry and energy are not always ideal. In a previous work, we created a Zr−O repulsive potential by only fitting to one highly symmetric phase, which is the cubic phase.[76] It turned out that the parameter can reproduce the bulk modulus of the cubic phase in perfect agreement compared to DFT (see also Figure S4 and Table S3 in the Supporting Information). This is because the Zr−O repulsive potential is trained to reproduce Zr−O bond lengths in the entire range of the cubic training set. By employing these parameters, the energy ordering of all three ZrO_2 phases is correct, but these parameters are excluded for further investigations due to the reasons explained below.

As mentioned earlier, the monoclinic phase is the most stable one observed at room temperature, followed by the tetragonal and cubic phases, the latter being stable in a high-temperature range. This is confirmed by our DFT calculations, yielding the energy ordering $E_m < E_t < E_c$, which agrees with previously reported PBE-PAW results.[77] Here, E_m, E_t, and E_c are the total energy of monoclinic, tetragonal, and cubic phase per ZrO_2 formula unit, respectively. E_t is higher than E_m by 0.1 eV/ZrO_2, whereas E_c is higher than E_t by 0.1 eV/ZrO_2. The DFTB2 energy ordering agrees with these DFT predictions regarding the tetragonal and cubic phases but incorrectly predicts the tetragonal phase to be lower than the monoclinic phase. Also, the energy difference for the tetragonal−cubic phase energy separation is slightly overestimated with 0.52 eV/ZrO_2. While it would be possible to refine the parameters aimed at reproducing the PBE energy ordering among all phases, other important quantities will be affected, in particular for the description of the oxygen migration barrier and the stability of the phases presented in the previous work.[76] If such parameters (*i.e.*, set 1 in ref 76) are employed in an MD simulation, the tetragonal phase spontaneously transforms to the monoclinic phase after very few MD steps even at temperatures close to 0 K (Figure S4), and the monoclinic−tetragonal phase transformation cannot be observed, likely due to the high DFTB2 energy barrier between these two phases. The long-range Zr−O repulsive potential (*i.e.*, set 2 in ref 76) can yield a perfect energy difference between the tetragonal and cubic phases along with a perfect agreement of the associated bulk moduli, but due to the negative value of the repulsive potential, the oxygen migration barrier is negative, which seems to be physically incorrect. Therefore, for our case, the exact ordering in terms of energy had to be sacrificed to achieve an adequate description of the tetragonal and cubic phases of ZrO_2. It is also worth mentioning that the energy differences of the phases are in the order of 0.1 eV/ZrO_2, which is very small and very sensitive to any approximation similar to the case of HfO_2 where the DFTB2 parameters fail to describe the correct energy ordering of the cubic and tetragonal phases[78] as well. Also, the well-known znorg parameter set fails to predict that wurtzite is the ground-state geometry of ZnO polymorphs.[47,48]

In our case, the test systems are even more complex. The most stable phase under standard conditions is the most complicated structure among the other standard atmospheric pressure phases employed to fit the Zr−O repulsive contribution, that is, the metastable phases (tetragonal and cubic), to yield a smooth potential without oscillations. Nevertheless, the current repulsive potential is able to describe the correct geometry for the high-temperature phases under the target conditions, in which case the energy ordering of the m-ZrO_2 and t-ZrO_2 phases has only a minimal impact on the simulation of YSZ.

Further tests are conducted for systems with native point defects, especially associated to oxygen vacancies. Oxygen ion mobility in YSZ has been related to the formation of vacancies in the oxygen sublattice. The defect formation energies for different charged states of the oxygen vacancy are calculated as follows

$$E^{\mathrm{f}}[V_{\mathrm{O}}^{q}] = E_{\mathrm{tot}}[V_{\mathrm{O}}^{q}] - E_{\mathrm{tot}}[\mathrm{bulk}] + \mu_{\mathrm{O}} + q(\epsilon_{\mathrm{F}} - E_{\mathrm{VBM}}) \quad (9)$$

$E_{\mathrm{tot}}[V_{\mathrm{O}}^{q}]$ is the total energy for a supercell containing an oxygen vacancy defect in a charged state given as q; $E_{\mathrm{tot}}[\mathrm{bulk}]$ is the total energy of the defect-free system; and μ_{O} is the chemical potential of oxygen. The fourth term on the right-hand side of eq 9 depends on the Fermi level ϵ_{F} relative to the valence band maximum E_{VBM} of the bulk system. The value for μ_{O} is not constant but varies for the O-poor and O-rich limits under a constraint given by the equilibrium conditions of ZrO_2. The μ_{O} values are in the range of $\mu_{\mathrm{O}}^{\mathrm{gas}} + 1/2\Delta E_{\mathrm{f}}^{\mathrm{ZrO_2}} \leq \mu_{\mathrm{O}} \leq \mu_{\mathrm{O}}^{\mathrm{gas}}$ with the lower and upper limits corresponding to O-poor and O-rich conditions, respectively. $\mu_{\mathrm{O}}^{\mathrm{gas}}$ is taken from the half of the total energy of the triplet oxygen dimer ($E^{\mathrm{O_2}}$), and $\Delta E_{\mathrm{f}}^{\mathrm{ZrO_2}}$ is the formation energy of ZrO_2 per formula unit, calculated as follows

$$\Delta E_{\mathrm{f}}^{\mathrm{ZrO_2}} = E^{\mathrm{ZrO_2}} - (E^{\mathrm{Zr}} + E^{\mathrm{O_2}}) \quad (10)$$

with E^{Zr} being the total energy of metallic Zr in the HCP phase divided by the number of Zr atoms in the unit cell, while $E^{\mathrm{ZrO_2}}$ corresponds to the total energy of a ZrO_2 polymorph divided by the number of ZrO_2 units in the respective unit cell. It should be noted that we did not aim for an "accurate" representation of the absolute defect formation energy since

https://doi.org/10.1021/acsomega.1c02411
ACS Omega 2021, 6, 20530−20548

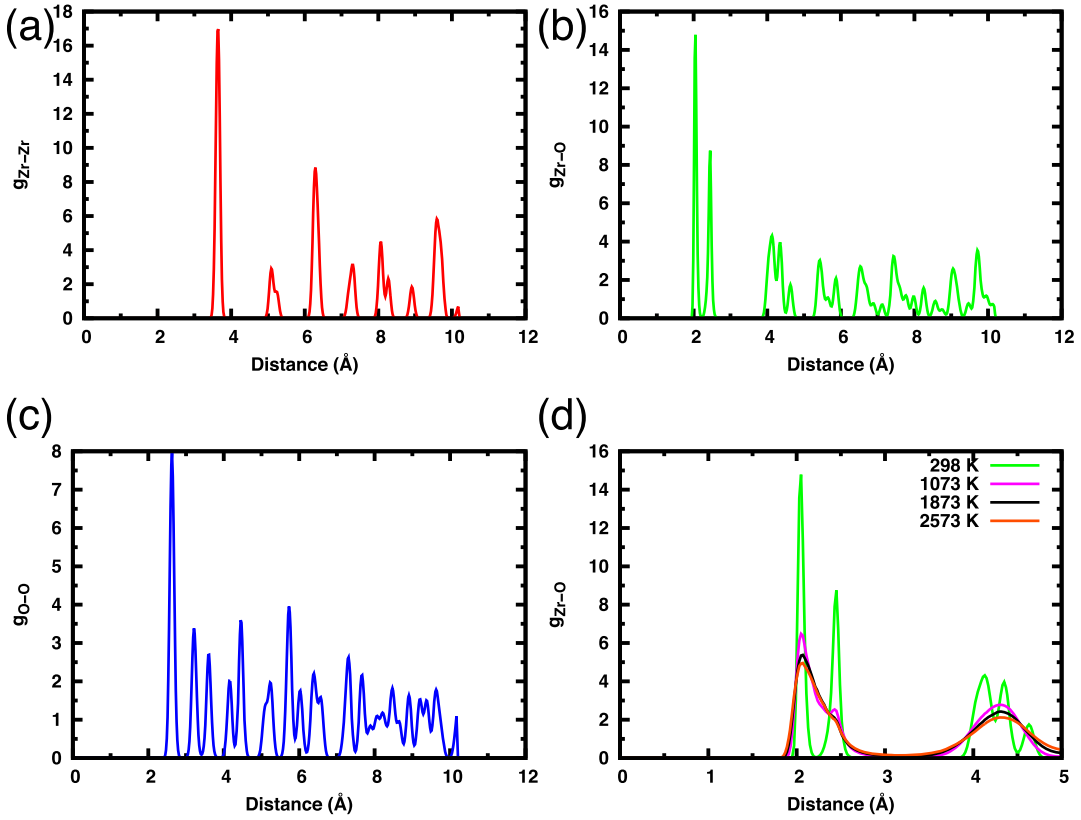

Figure 5. (a–c) Ion–ion pair distribution functions for ZrO_2 at 298.15 K. ZrO_2 converges to the tetragonal phase at room temperature as expected. (d) Comparison of g_{Zr-O} obtained under different thermal conditions.

DFTB2 tends to overestimate this property.[79] Instead, the performance of the Zr–O parameters is assessed against the relative stability of the defect with respect to the Fermi level. Thus, no further correction has been employed to take size and charge effects inside the defective unit cell into account. Only, an energy correction of 1.36 eV is employed to adjust the binding energy of O_2 from PBE-based calculations.[80] The bulk supercells are modeled using a 3 × 3 × 3 unit cell expansion for *m*-ZrO_2 and *c*-ZrO_2 (324 atoms) and 4 × 4 × 4 for *t*-ZrO_2 (384 atoms). To create the supercell containing an oxygen point defect, one oxygen atom has been removed from the respective systems. For all calculations, charge states of 0 (neutral state) and +2 are considered.

The introduction of vacancies in *m*-ZrO_2 and *t*-ZrO_2 does not significantly alter their structure and symmetry with only slight geometric relaxations close to the vacancy site. However, full atomic relaxation of the defective *c*-ZrO_2 will lead to stabilization *via* a phase transition to *t*-ZrO_2. For this reason, the defect formation energy for *c*-ZrO_2 has been determined for the unrelaxed geometry. Figure 4 shows the formation energy of oxygen vacancy defects for the considered ZrO_2 polymorphs. All vacancies become stable at neutral states when the Fermi level is close to the conduction band, as shown earlier based on DFT results. The transition levels $\epsilon(+2/0)$ for *m*-ZrO_2, *t*-ZrO_2, and *c*-ZrO_2 are found at 1.8, 2.5, and 3.0 eV, respectively. The stability and the transition levels are in good agreement with DFT results where values of 2.9 and 3.2 eV have been reported for $\epsilon(+2/0)$ in the case of *t*-ZrO_2 and *c*-ZrO_2, respectively.[80,81] Unfortunately, there is a lack of data for the defect formation energy for *m*-ZrO_2. In general, the oxygen vacancy formation is likely to occur under low-oxygen conditions.

In order to further verify the accuracy of the developed potential, an MD simulation at 298.15 K and 1.013 bar was carried out. Initially, the starting simulation cell was taken from the cubic ZrO_2 structure with a slight displacement of the atoms from the ideal crystal position. However, from the analysis of the trajectory after several ps of sampling, the atoms in the cubic simulation box align themselves to the tetragonal structure even if an isotropic pressure coupling is applied, verifying that the tetragonal phase is more stable than the cubic phase, as observed in the experiment and from the previous *E*-V curve. Therefore, further MD simulations and analyses were carried out employing a semi-isotropic pressure coupling (*i.e.*, independent scaling of the lattice vectors but no variation in the lattice angles) on zirconia. The MD simulation was subject to 2 ps of equilibration followed by a sampling period of 6 ps for 4 × 4 × 4 unit cell expansion. The lattice parameters and temperature have reached equilibrium within this simulation period, as shown in Figure S5. An average density of 6.01 kg dm^{-3} has been observed, which is in good agreement with the experimental value of 6.09 kg dm^{-3}.[82] The average lattice parameters obtained from the sampling period are a = 3.603 Å and c = 5.246 Å, which are also in good agreement with the experimental values.[83]

The RDFs of tetragonal zirconia are depicted in Figure 5a–c. The Zr–O RDF shows that there are two sharp peaks at 2.08 and 2.44 Å. These peaks correspond to the Zr–O first nearest neighbor distances in the tetragonal crystal structure.[84] In order to investigate the effect of the size of the simulation box, an MD simulation at 298.15 K and 1.013 bar for a smaller 2 ×

https://doi.org/10.1021/acsomega.1c02411
ACS Omega 2021, 6, 20530–20548

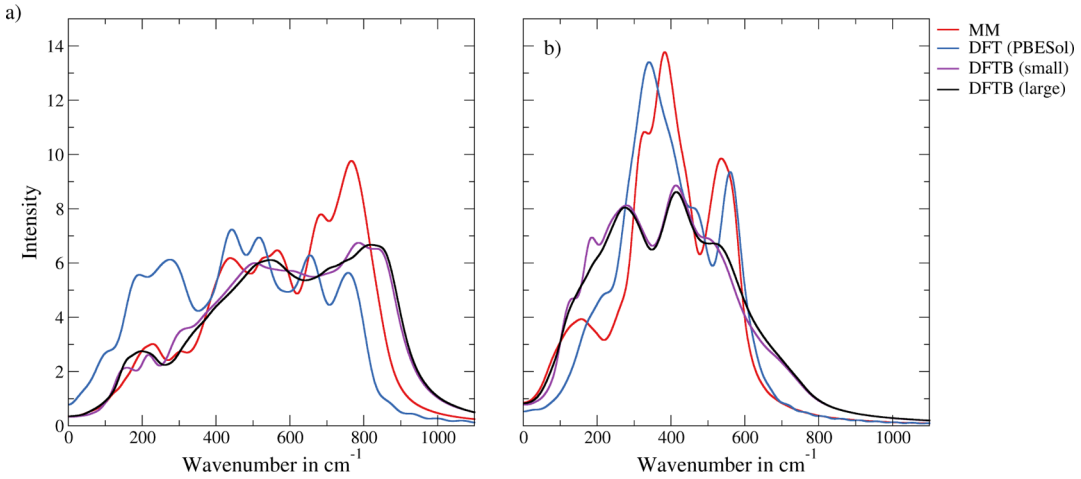

Figure 6. Comparison of the vibrational power spectrum of (a) *t*-ZrO_2 and (b) *c*-Y_2O_3 obtained at DFT, DFTB2, and MM levels. While the intensities of the bands are not directly comparable due to the FT step in the analysis, the highly similar range from 100 to 1000 cm^{-1} implies similar underlying effective force constants in the respective description.

2 × 2 unit cell expansion containing a total of 96 atoms has been carried out. It can be seen from Figure S6 that the RDFs of the smaller system overlap the RDFs of the larger system. Since there is no apparent size effect on the RDFs for the ZrO_2 systems, further simulations have been carried out employing smaller systems since it enables longer sampling periods.

In order to verify the suitability of the currently developed parameters at elevated temperatures, simulations at 1073.15, 1873.15, and 2573.15 K of the 2 × 2 × 2 system have been carried out for a total sampling period of 60 ps. As seen from Figure 5d, no shift in the peaks is observed in the Zr−O pair distributions, which indicates that there are no structural changes occurring along the simulation. Only a broadening of the peaks linked to a reduction in intensity is observed, resulting from the increased thermal state of the systems.

To provide an additional verification of the potential model, a DFT-based simulation at the PBEsol level has been carried out to compare the vibrational properties of the system. Due to the dramatically increased computational demand of QM-based simulations, only a short simulation time of 2000 MD steps (4 ps) was achieved after 1000 steps of equilibration. Nevertheless, this short sampling period is sufficient to evaluate the vibrational power spectrum of the system. Figure 6a shows a comparison between the spectra obtained at 298.15 K from the QM- and DFTB-based descriptions of *t*-ZrO_2. In all cases, a similar range in the wavenumbers from 100 to 1000 cm^{-1} is observed. Experimental infrared spectra reveal that the characteristic Zr−O bond vibrational wavenumber lies in a range of 164−650 cm^{-1}.[85] The predicted DFTB2 absorption peaks occur at 151, 303, 500, and 800 cm^{-1}. Our QM-based calculations predict the absorption peaks in a range of 200−790 cm^{-1}. Other DFT calculation predicts a comparably low-frequency absorption peak with the experimental data with 153 cm^{-1} but overestimating the high-frequency absorption peak with 743 cm^{-1}.[86] By these comparisons, DFTB2 results agree reasonably with the reference data.

In order to obtain suitable spectra, the FT step is typically subject to a decaying window such as an exponential function. While wavenumbers of the individual modes are virtually unaffected by the application of an exponential window, the intensities show a strong dependence and, therefore, cannot be directly compared between different levels of theory. Furthermore, since all vibrational modes are present in the underlying VACF, convoluted spectra of all associated bands are obtained. Different levels of theory are prone to yield different intensity−width ratios of the associated bands, and thus, the intensity of different power spectra is not directly comparable. Other factors that may also influence the intensity of individual bands are system size and simulation length. Especially, in the case of the highly demanding MD simulation at the DFT-level (PBEsol functional), the simulation time is comparably short. In addition, every DFT formulation is subject to a number of approximations, implying that the DFT MD simulation does not necessarily represent the best possible result. Therefore, this kind of analysis only provides data on the spectral range, which is highly similar over all considered levels of theory even in the case of the recently published MM model.[87] An example of a MM description showing an inadequate spectral range obtained in a previous study[87] is shown in the Supporting Information, Figure S7. Here, the potential model labeled as MM-2 shows a strongly deviating range of wavenumbers. Since the masses of all atoms in the system are identical in the respective simulations, too high wavenumbers imply an increased effective force constant. Since the latter is dependent on the second derivative of the potential energy with respect to the nucleic coordinates at the equilibrium position, the deviation arises from an inadequate (too steep) potential energy surface. Thus, on the other hand, a coinciding range in wavenumbers obtained at different levels of theory implies that the effective force constants and hence the potential energy are highly similar.

To calculate the effective force constant at 0 K, direct phonon calculations were also carried out at the DFTB2 level. The vibrational density of states is presented in Figure S8. The results show that the *c*-ZrO_2 has an imaginary (*i.e.*, negative) frequency region, while the *t*-ZrO_2 contains all positive frequency. These negative frequency modes are responsible for the cubic−tetragonal phase transition, in agreement with the DFT, ref 77. However, we have to admit that by this direct phonon calculations, the frequency of *t*-ZrO_2 is blue-shifted to the high-frequency region, and there is even a "vibrational band gap". It means that the tetragonal potential energy surface is too steep at 0 K. We have addressed this issue since we have to put more weight in the parameterization to force the

https://doi.org/10.1021/acsomega.1c02411
ACS Omega 2021, 6, 20530−20548

stabilization of the tetragonal phase. Another problem related to this is that the direct phonon calculations are generally very sensitive to the numerical accuracy of the atomic forces. We have tested the converged results with respect to *k*-point sampling, supercell size, and the self-consistent charge threshold. This does not seem to be the problem at the elevated temperature since the FT spectra of *t*-ZrO_2 are in reasonable agreement with the experimental ones. We believe that this discussion will be helpful to the DFTB developer community for future DFTB parameter development.

3.2.3. Y_2O_3. The increased complexity of the Y_2O_3 structure seems to bring extra difficulty to the parameterization of the Y−O repulsive potential. The *c*-Y_2O_3 (space group $Ia\bar{3}$) has the experimental lattice parameter of 10.604 Å.[88] The Y−Y bond distribution from the experiment shows that the Y−Y first nearest neighbor bond lengths contain two nearly identical bonds at 3.515 and 3.532 Å, while the second nearest neighbor bond distances are 3.999 and 4.014 Å. We confirmed that creating a Y−Y repulsive potential with a cutoff shorter than 3.5 Å indeed yields an unreasonable geometry for bulk Y HCP. For this reason, the Y−Y and Y−O repulsive interactions have to be carefully generated simultaneously to match the description of both bulk Y and Y_2O_3, while keeping the Y−Y cutoff distance before the second nearest neighbor distance to avoid the repulsive potential overshoot.

Table 5 lists key bulk properties of *c*-Y_2O_3 obtained from the current DFTB2 parameters in comparison with experimental values and present PBE-PAW calculations. The current Y−Y and Y−O parameters are able to reproduce the lattice parameter *a* in excellent agreement with the experimental value, being increased by only 0.007 Å compared to the experimental value but shorter than the value obtained at the PBE-PAW level. PBE-PAW results show that the Y−Y first neighbor bond lengths are 3.532 and 3.547 Å, while the second neighbor distances are found at 4.020 and 4.035 Å. The corresponding DFTB2 results show that the Y−Y first neighbor bond lengths are slightly overestimated by 0.060 and 0.053 Å compared to the PBE-PAW results. Conversely, the Y−Y second nearest neighbor distances are underestimated by 0.102 and 0.111 Å in the DFTB2 case. A similar analysis can also be conducted for the Y−O distances. The Y−O nearest neighbor distances consist of four nearly identical bonds at 2.242, 2.273, 2.287, and 2.328 Å based on the experimental results, while PBE-PAW calculations yield the associated bond lengths of 2.258, 2.278, 2.295, and 2.345 Å. In the DFTB2 case, the first two Y−O bonds are shorter by 0.082 and 0.036 Å, while the second set of bonds is enlarged by 0.030 and 0.113 Å. Nevertheless, by performing the symmetry operations to the Wyckoff positions to the atomic fractional coordinates of the atoms from the DFTB2-optimized geometry (Table S4), the $Ia\bar{3}$ space group of the *c*-Y_2O_3 is preserved. This implies that the generated parameters can adequately represent the geometry and symmetry of this system. The Mulliken charges of Y and O of the optimized geometries are tabulated in Table S2. The average Mulliken charges for Y and O in Y_2O_3 are *ca.* +0.6 and −0.4, respectively. The magnitude of the Mulliken charges is also lower than that of the assumed FOS of Y and O, being +3 and −2, respectively, similar to the case of ZrO_2.

Table 5. Selected Bulk Properties of Cubic Yttria Obtained from DFT, DFTB2, and Experiment

parameter	PBE-PAW[a]	DFTB2	experiment
a (Å)	10.655	10.610	10.604[88]
B_0 (GPa)	136	142	148.9 + 3.0[125]

[a]Present study.

The *E*−*V* curve resulting from the current DFTB2 parameters is hard to distinguish from the *E*−*V* curve computed at the PBE-PAW level (see Figure 7). This similarity can also be seen from the values of the bulk modulus, B_0, which only differs by 6 GPa. Furthermore, the bulk modulus calculated at the DFTB2 level is very close to the experimental value. As pointed out earlier, fitting to only one phase of high symmetry, (*e.g.*, cubic) often yields near-perfect agreement with the reference data, given that the reference QM level is sufficiently accurate.

To also validate the currently developed DFTB parameters for the Y−O interactions, an MD simulation for cubic Y_2O_3 has been carried out as well. The average density of cubic Y_2O_3 obtained from the simulation is 4.95 kg dm^{-3}, which is in excellent agreement with the experimental values of 5.01 kg dm^{-3}.[88] The average lattice parameter obtained from the sampling period is *a* = 10.651 Å.

Figure 8a−c shows the ion−ion pair distribution functions at 298.15 K. A good agreement in the Y−Y and Y−O bond lengths from the static calculations is observed. Similar to the case of zirconia, simulations at elevated temperature have been carried out. Again, the expected peak broadening along with a reduction in the respective intensities is the only structural change observed in these simulations (Figure 8d).

In the case of *t*-ZrO_2, the spectra obtained for *c*-Y_2O_3 show similar characteristics in the range of 100−600 cm^{-1} (Figure

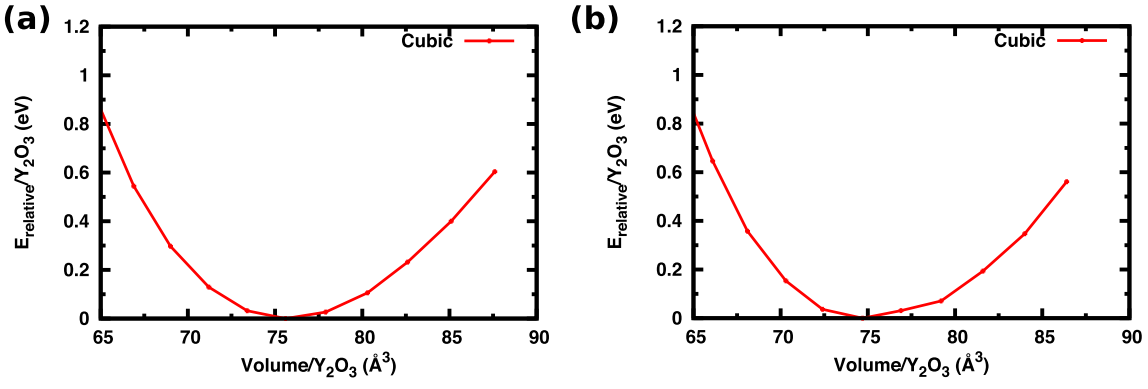

Figure 7. Relative energy *vs* volume per Y_2O_3 unit for cubic yttria obtained using (a) PBE-PAW and (b) DFTB2.

https://doi.org/10.1021/acsomega.1c02411
ACS Omega 2021, 6, 20530−20548

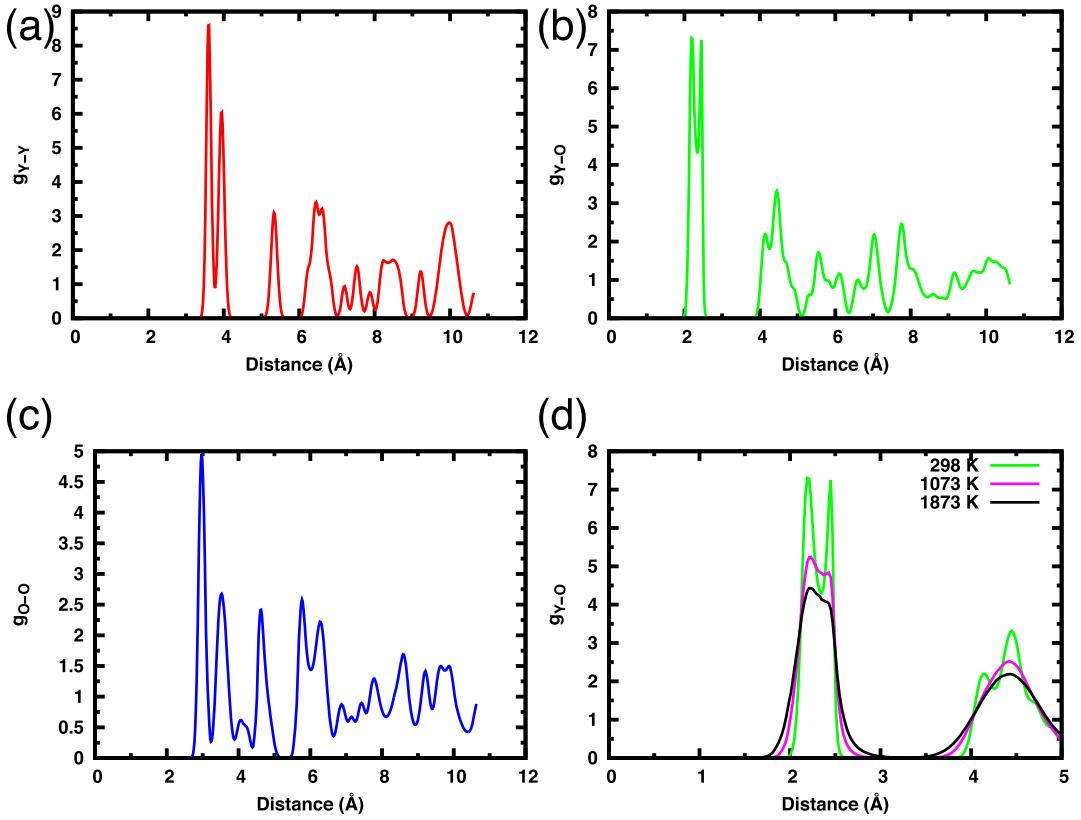

Figure 8. (a–c) Ion–ion pair distribution functions for Y_2O_3 at 298.15 K. (d) Comparison of g_{Y-O} obtained under different thermal conditions.

6b). Experimental infrared spectra reveal that the characteristic Y–O bond vibrational wavenumber lies in a range of 400–600 cm^{-1}.[89] Results agree reasonably with the experimental results, where the peaks occur at 414 and 532 cm^{-1}. As before, the main focus of this analysis is to verify whether the different computational methods yield a similar spectral range or if significant outliers in the bands are present (see also the Supporting Information, Figure S7).

3.2.4. YSZ. In order to test the newly constructed DFTB2 parameters for the Zr–Y–O interactions developed in this work, short-time MD simulations of two representative YSZ*n* systems (n = 4 and 12) have been carried out. The main focus was to verify if addition of yttrium oxide can indeed stabilize the cubic phase of YSZ. The two systems have been constructed based on a 4 × 4 × 4 expansion of a *c*-ZrO_2 unit cell followed by random substitution/deletion of the respective ions (see Table 2 for details on the number of included ions). A total of 3000 MD steps (6 ps) have been performed for sampling, following an equilibration period of 1000 MD steps (2 ps) in the *NPT* ensemble (298.15 K, 1.013 bar). The temperature has reached equilibrium, as shown in Figure S9.

Based on the respective ion–ion pair distributions and lattice parameters obtained for the two systems depicted in Figures S9–S11, it can be concluded that both systems remained in the cubic phase under standard conditions. The respective densities in the case of YSZ4 and 12 obtained from the DFTB MD simulations are given as 5.94 and 5.82 kg·dm^{-3}, corresponding to an effective lattice constant for a single unit cell of 5.155 and 5.171 Å, respectively. Due to the often porous or/and nanocrystalline nature of YSZ compounds, accurate estimations of the density/lattice constants of a particular YSZ composition are difficult to obtain from the literature. Nevertheless, the observed densities appear to be in good agreement when compared to the theoretical density of YSZ8, reported as 5.958 kg·dm^{-3},[90] while being lower than the extrapolated theoretical density of cubic ZrO_2, given as 6.01 kg·dm^{-3}.[82]

Similarly, the lattice constants obtained in the DFTB MD simulations proved to be in good agreement with the equation of states derived by Suciu *et al.*[91] In this work, a linear relation between the lattice constants a_n of YSZ*n* and the respective molar percentage n of Y_2O_3 was derived *via* a least-square fit to experimental reference data reported by Kawata and coworkers[92] based on Y-89 magic angle spinning nuclear magnetic resonance spectroscopy

$$a_n = 5.106\ \text{Å}\cdot(1 + 7.940 \times 10^{-4} n) \quad (11)$$

The respective values obtained from eq 11 for YSZ4 and 12 are 5.122 and 5.155 Å. The associated absolute deviations of the DFTB MD results amount to 0.033 and 0.017 Å, corresponding to relative deviations of 0.64 and 0.32% for YSZ4 and 12, respectively. Keeping in mind that the DFTB MD simulations for the two systems have been carried out for only a single configuration (based on randomized substitutions/deletions of Zr and O ions in the parent ZrO_2 lattice) and the fact that the relation by Suciu *et al.* is based on a linear least-square fit, the experimental and simulated lattice constants have been considered to show near-perfect agreement.

Due to the comparably low simulation temperature and short sampling time, no migration of oxygen ions throughout the solid was observed. The latter is of course one of the remarkable features of YSZ compounds, which will be explored

https://doi.org/10.1021/acsomega.1c02411
ACS Omega 2021, 6, 20530–20548

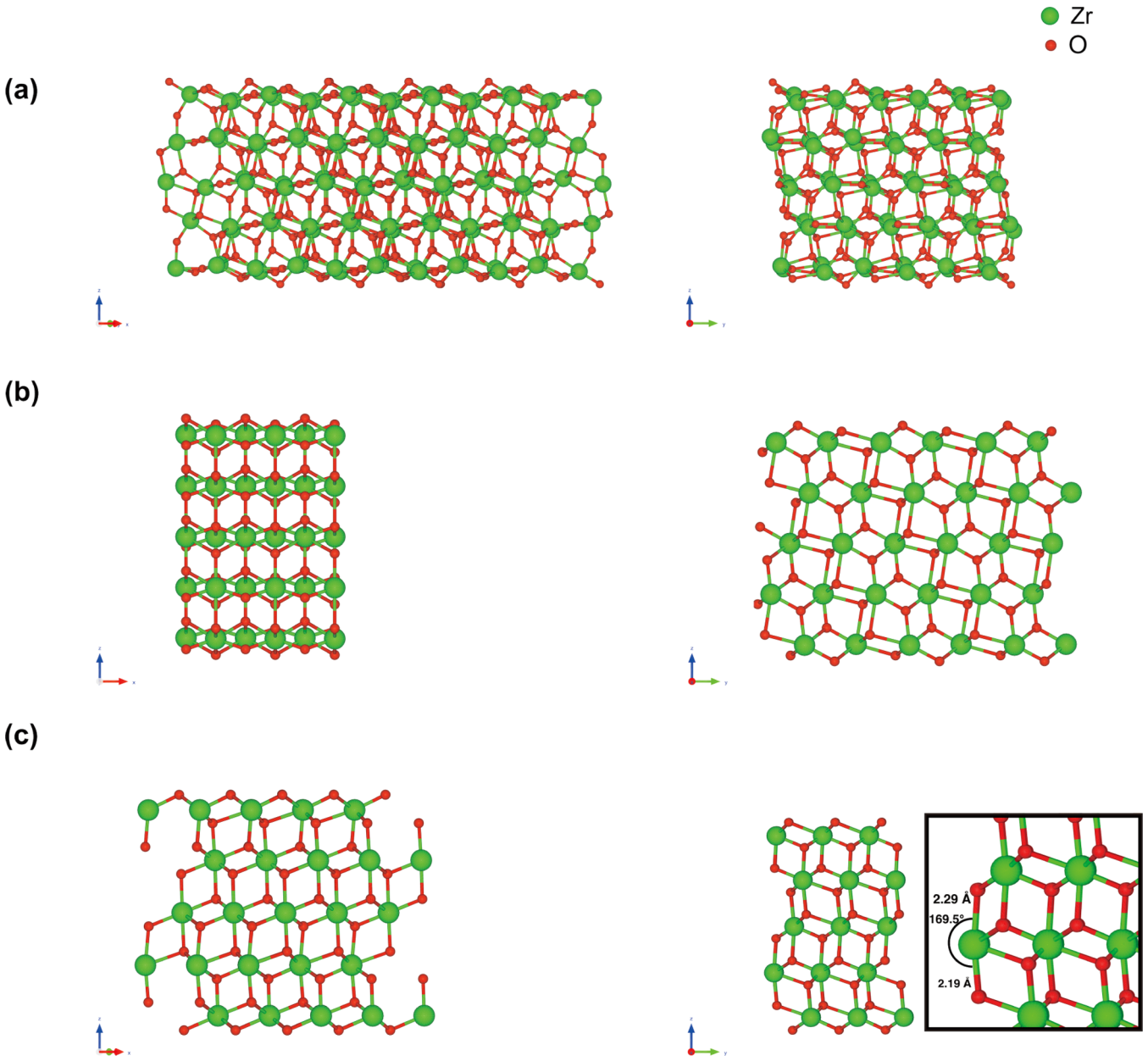

Figure 9. Different views of the optimized structure of 2d-periodic (a) *m*-ZrO_2(−111), (b) *t*-ZrO_2(101), and (c) *c*-ZrO_2(111) model systems obtained at the DFTB2 level of theory. The *z*-axis represents the non-periodic direction. The unit cells are expanded to three units to each periodic direction for clarity. The inset shows the O−Zr−O angle deformation of *c*-ZrO_2(111) compared to the ideal value of 180°.

in detail in future work. The newly derived Zr−Y−O DFTB2 parameterization presented and validated in this contribution thus forms a reliable basis for these investigations, which will enable simulations at different temperatures and for different YSZ compositions, considering both the molar percentage and different randomizations of the individual systems.

3.3. Properties of the Low-Index Surfaces. *3.3.1. ZrO_2.* One of the main motivations for developing new DFTB2 parameters is to describe reactions or processes catalyzed by zirconia and YSZ. Such processes take place on the metal oxide surface, and thus, a chemically correct description of the respective surfaces becomes necessary. The free-standing surfaces of zirconia have been studied both experimentally[93] and theoretically employing a number of QM-based methods.[94−97] In addition, interactions of several molecules such as hydrogen,[98] water,[99−101] carbon dioxide,[101] sulfuric acid,[102] and so forth on several zirconia surfaces have been studied theoretically. It appears from the experimental results that the tetragonal (101) facet is the most abundant surface of the tetragonal phase, while the (−111) plane is the most abundant surface in the monoclinic case.[93]

Theoretical results further confirm the stability of these facets by the values of the respective surface energy. Christensen and Carter[95] performed systematic studies on the different surfaces for all three zirconia phases at the Perdew-Zunger level, identifying (101) and (−111) as the most stable surface planes for tetragonal and monoclinic zirconia, respectively. Recently, Ricca *et al.* discovered that the (111) termination is the most stable plane for the cubic phase based on calculations performed at the PBE0 level of theory. From these results, we focus on the most stable surfaces of the monoclinic, tetragonal, and cubic phases, namely, monoclinic

https://doi.org/10.1021/acsomega.1c02411
ACS Omega 2021, 6, 20530−20548

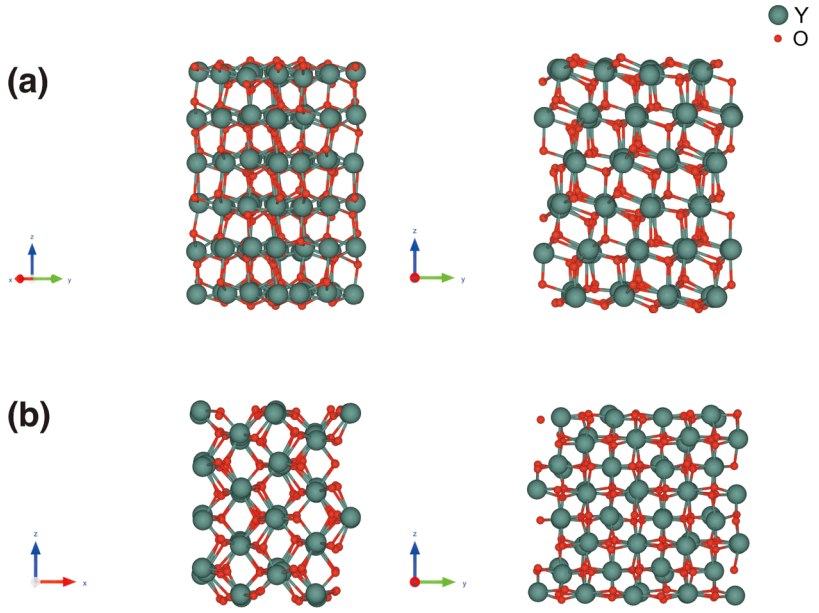

Figure 10. Different views of the optimized structure of 2d-periodic (a) *c*-Y_2O_3(111) and (b,a) *c*-Y_2O_3(110) model systems obtained at the DFTB2 level of theory. The *z*-axis represents the non-periodic direction.

(−111), tetragonal (101), and cubic (111) surfaces, respectively. Previous studies also show that the most stable zirconia surfaces are oxygen-terminated.[96,97] Therefore, only oxygen-terminated planes are considered in this work.

The surfaces were constructed by cleaving the bulk phases along the desired direction. Herein, the surface energy is reported from the fully relaxed surface model with the following equation

$$E_{surf} = \frac{E_{tot} - nE_{bulk}}{2A} \quad (12)$$

where E_{tot} is the total energy of the surface model, n is the number of layers, E_{bulk} is the energy of the bulk phase with an equivalent number of atoms of a 1-layer surface, and A is the surface area. In a sufficiently large slab, the surface energy should converge to the energy of the bulk system.

The fully relaxed monoclinic (−111) and tetragonal (101) surface for a 5-layer model is shown in Figure 9a,b. The surface structures are in agreement with the bulk configuration with only a slight structural relaxation close to the vacuum interface. For example, the first neighbor Zr−O bond lengths in bulk *t*-ZrO_2 are found as 2.08 and 2.44 Å. The Zr−O bonds of the outermost *t*-ZrO_2 (101) layer slightly relax to 2.01 and 2.42 Å, while the bond lengths observed in the inner layers coincide with the bulk Zr−O distances. Thus, the structure relaxes both upward and downward along the non-periodic *z* direction, which implies that the upper- and bottommost layers have the same surface area, *A*, in eq 12. The DFTB2-calculated surface energies of the monoclinic (−111) and tetragonal (101) surfaces converge to 1.916 and 2.264 J m^{-2}, respectively, within five layers without any noticeable oscillation. As a comparison, we calculated the surface energy of the tetragonal (101) surface at the PBE-PAW level, and the value converges to 1.021 J m^{-2}, which is in agreement with previous calculations at the PBE-PAW level, 1.090 J m^{-2}, by Eichler and Kresse[96] but lower than that obtained at the PBE0/ECP level, 1.512 J m^{-2}.[97] The value of the surface energy obtained at the DFTB2 level is somehow larger than the previous and current theoretical calculations. This is a general trend in DFTB, as the cohesive energy is usually overestimated[103] (*i.e.*, the energy required to atomize from the bulk phase), which consequently leads to an overestimation of the surface energy.

However, different results were obtained for the cubic (111) surface. There seems to be a rather significant change in the surface structure at the DFTB2 level of theory. As seen from Figure 9c, the main geometry change after relaxation is the O−Zr−O angle. The angle changes from the ideal bulk value 180 to 170° for all of the layers. The geometry resembles the geometry of the tetragonal (101) surface. This may be because the tetragonal−cubic phase transformation is barrierless and the cubic phase is less stable than its tetragonal counterpart.[104] Upon relaxation, the energy is transformed to that of the lower energy surface. The instability of the cubic surface was also observed in an earlier LDA-PAW study by Christensen and Carter, in which all cubic surfaces immediately transform to a tetragonal surface after ionic and cell relaxation.[95] In the current PBE-PAW reference calculations, the cubic symmetry of the relaxed cubic (111) surface can be preserved; however, no converged surface energy is observed. In this case, the relaxed surface energy scales with the layer size. Previous studies report that the cubic (111)-terminated plane is the most stable surface of zirconia with converged surface energy-employed calculations at the HF and hybrid density functional, that is, PBE0 level of theory,[97,105] and thus, the properties of this surface seem to depend strongly on the employed level of theory. Nevertheless, while the currently developed DFTB2 parameters may have several drawbacks for the cubic surface, they are suited to study processes on the monoclinic and tetragonal surfaces. Most of the catalytic reactions are also expected to take place on the tetragonal surface.[98,102] In addition, by comparing the magnitude of the surface energy, the monoclinic (−111) surface is more stable than its tetragonal (101) counterpart, in agreement with DFT results.[97]

3.3.2. Y_2O_3. To complement the results of the ZrO_2 surfaces, we also evaluated the performances of the current DFTB2 parameters on the surface structures of Y_2O_3. The surfaces of pure Y_2O_3 received less attraction from the theoretical point of

https://doi.org/10.1021/acsomega.1c02411
ACS Omega 2021, 6, 20530−20548

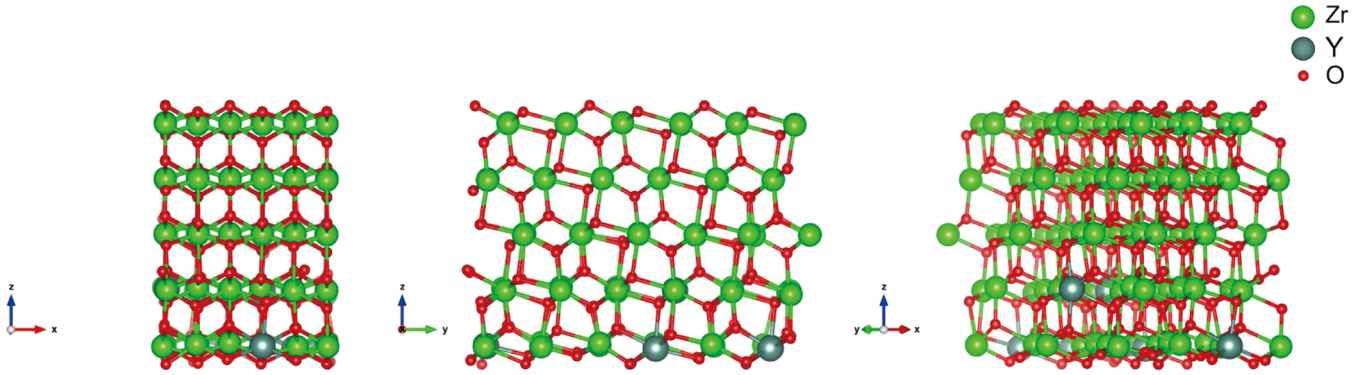

Figure 11. Different views of the optimized structure of a 2d-periodic YSZ model system obtained at the DFTB2 level of theory. The *z*-axis represents the non-periodic direction.

view, but several experimental studies on the adsorption of small molecules on pure Y_2O_3 exist.[106−110] The authors highlighted the importance of the oxide surfaces in catalytic and/or SOFC activities. However, no structural or plane surface information was obtained from experimental or theoretical calculations. As a model, we chose the Y_2O_3 (111)- and (110)-terminated surfaces since the experimental X-ray diffraction pattern of bulk Y_2O_3 shows two prominent reflexes associated to the (222) and (440) direction, which implies that the preferred growth orientation of Y_2O_3 are the (111) and (110) planes.[111]

Due to the relatively large unit cell of *c*-Y_2O_3, the surface energy convergence test for 1 × 1 Y_2O_3 surface can only be achieved by an integer multiplication of 2- and 4-layers for the (111) and (110) surfaces, respectively. For this reason, surface energy calculations at the PBE-PAW level of theory proved computationally too demanding in the DFT case.

The DFTB2 results show that E_{surf} converges to 1.748 and 2.123 J m^{-2} in the case of *c*-Y_2O_3 (111) and (110), respectively. By comparing the magnitude of E_{surf}, DFTB2 predicts that the *c*-Y_2O_3 (111) surface is more stable than its (110) counterpart. These findings agree well with the experimental results, indicating that at low temperatures, the (111) growth orientation is preferred, while the (110) direction dominates at higher temperatures.[112]

The surface stability can also be judged from the geometrical properties. Different from the case of zirconia surfaces, it is expected that the only existing cubic phase of Y_2O_3 will not be subject to any physical phase transformation. As seen from Figure 10 for the 6-layer (111) and 8-layer (110) surfaces, the system does not show any significant relaxation after cleaving the surface. The Y−O bond length deviates 3−5% compared to the Y−O bond lengths of the bulk phase on the outermost layer. It appears that the current DFTB2 parameters are also well suited to study the processes on Y_2O_3 surfaces.

3.3.3. YSZ. The successful description of the tetragonal (101) surface prompts us to further test the currently developed DFTB2 parameters on the YSZ surface model. For the current work, the tetragonal YSZ (101) surface was constructed from a 5-layer 3 × 3 unit cell expansion of the tetragonal ZrO_2 (101) surface, yielding a total of 270 atoms. Then, six Zr atoms were randomly replaced with Y, and three O atoms were removed from the structure. Thus, a total of 267 atoms were obtained in the final structure, which represents approximately 3% mol Y_2O_3 in YSZ. Figure 11 reveals that the structure of the tetragonal YSZ (101) surface is close to that of the surface of tetragonal ZrO_2 (101). The only significant structural change is observed in the Zr−O bonds and Zr−O−Zr angles close to the oxygen vacancy, which seems to be quite reasonable. Although we currently do not consider the position of the Y atoms and the oxygen vacancies, it is likely that higher concentrations of the oxygen vacancy will not significantly alter the tetragonal symmetry of the surface, as seen also from the MD results of bulk YSZ, discussed below.

3.3.4. Dynamics of ZrO_2 and Y_2O_3 Surfaces. The currently developed Zr−Y−O parameters provide sufficient accuracy for the description of the geometries of the *t*-ZrO_2, *c*-Y_2O_3, and *t*-YSZ (101) surfaces, as presented in an earlier section. For future simulations involving the solid−vacuum interface, for example, in studies of surface-catalyzed reactions, the stability of the surface at the operating temperature is also necessary. It is expected that above 0 K, the surface does not undergo surface reorganization. For this reason, the surface stability of the model systems above 0 K is also evaluated *via* MD simulation. The surface models are subject to at least 30 ps simulation time at room temperature (298.15 K). The *t*-ZrO_2 (101) and *c*-Y_2O_3 (110) are taken as representative examples.

Figure S12 depicts the room temperature structures of *t*-ZrO_2 (101) and *c*-Y_2O_3 (110) models after 30 ps simulation time. It appears that the structures of both of the model surfaces retain the bulk symmetry while also being in agreement with the geometries obtained from the static geometry optimization presented in Section 3.3. Following this initial evaluation, it is expected that other surface models, considered presently, that is, *m*-ZrO_2 (−111), *c*-Y_2O_3 (111), and *t*-YSZ (101), will not undergo surface reorganization and maintain the bulk geometry at elevated temperatures.

4. DISCUSSION

This work presents the DFTB2 parameterization of ZrO_2 and Y_2O_3, focusing on the repulsive potential parameterization, attempting to satisfy several physical constraints such as geometry, energy, and vibrational spectra. The major highlight of the present work is the transferability of the Zr−O repulsive potential among the different ZrO_2 polymorphs. It has been demonstrated that the short-range Zr−O potential can yield correct geometries and energy ordering of *t*-ZrO_2 and *c*-ZrO_2. However, a slight displacement of the oxygen atoms in *c*-ZrO_2 induced by a native point defect formation or thermal vibration will eventually induce a spontaneous phase transition from the cubic phase to the tetragonal. This observation appears to be correct from both the experimental and theoretical points of view since the tetragonal−cubic phase transformation is

https://doi.org/10.1021/acsomega.1c02411
ACS Omega 2021, 6, 20530−20548

barrierless.[104] However, it can also be explained based on the relationship between the Zr−O repulsive potential range and the Zr−O bond length in the training set.

As seen in Figure S13, the Zr−O nearest neighbors in *c*-ZrO_2 cover a range from about 2.10 to 2.33 Å. The first and second nearest neighbors of *t*-ZrO_2 are found in the range of 2.07−2.10 and 2.17−2.50 Å, respectively. The gap between the first and second neighbors in the training set data for the *t*-ZrO_2, from 2.10 to 2.17 Å, is filled by the repulsive potential from the *c*-ZrO_2. In this sense, the repulsive potential between about 2.00 and 2.10 Å is associated to *t*-ZrO_2, while the range of 2.10−2.17 Å is associated to *c*-ZrO_2. The next interval in the range of 2.17−2.33 Å is associated to both *c*-ZrO_2 and part of *t*-ZrO_2, while the final range of 2.33−2.50 Å is associated exclusively to *t*-ZrO_2 (see Figure S13). By constructing the Zr−O repulsive potential in such a manner, the equilibrium geometry for *t*-ZrO_2 and *c*-ZrO_2 corresponds to different regions in the repulsive potential. Constraining the geometry to a cubic symmetry, a delicate force balance close to the *c*-ZrO_2 equilibrium geometry enables the stabilization of the cubic phase. This is evident as the force calculations in the *c*-ZrO_2 case, in which all atomic force components are found to be below 1×10^{-4} E_h/a_0, which is smaller than the geometry convergence threshold. However, since the cubic region is partially overlapping with its tetragonal counterpart, the repulsive interaction can no longer resolve the phase, as the forces are imbalanced whenever atomic displacements occur. For this reason, the cubic structure readily transforms to the tetragonal phase.

Throughout this study, the "traditional" short-range 2-body repulsive contribution has been employed. This 2-body repulsive term is independent with respect to the coordination number and chemical hybridization. In addition, this short-range repulsive potential partly contributes to overbinding. For complicated bonding situations and in particular for solid-state systems where coordination numbers are high, developing a more flexible repulsive potential capable of describing all physical quantities would involve going beyond the traditional 2-body repulsive potentials and moving toward promising many-body formulations, as recently described.[113,114] However, these novel approaches have been applied to a very limited range of systems as of yet, and we feel that the currently employed DFTB2 methods and developed parameters provide adequate accuracy compared to DFT and experimental data for the problem at hand, and these can be further employed for large-scale calculations in which more demanding computational approaches are not affordable.

5. CONCLUSIONS

A new set of DFTB2 parameters mainly targeted to describe the bulk and surface properties of ZrO_2 and Y_2O_3 has been developed. The newly developed DFTB2 parameters have been shown to provide a qualitative agreement of the phase stability and energy ordering of the high-temperature phases of ZrO_2 at standard atmospheric pressure, namely, cubic and tetragonal phases, for which the energy ordering is as follows: $E_t < E_c$. The structural parameters of the bulk phases and several surface models of ZrO_2 and Y_2O_3 are in good agreement with experimental and reference DFT results. In addition, MD simulations of bulk ZrO_2 and Y_2O_3 provide an assessment of the phase stability as a function of temperature. It is revealed that the tetragonal phase of ZrO_2 and cubic Y_2O_3 are stable at room temperature up to relatively high temperatures (>1800 K) and do not show any tendency to undergo a phase transformation. In addition, the analysis of the vibrational power spectra obtained *via* FT of the associated velocity autocorrelation functions yields a highly similar spectral range in the region from 100 to 1000 cm^{-1} when compared to all-DFT and classical MD simulations, implying that the underlying potential energy surface has very similar properties. Further MD simulations of YSZ*n* (n = 4 and 12) revealed that the cubic phase is indeed stabilized upon addition of Y_2O_3, with the respective average lattice constants being in good agreement with experimental reference data.

The emerging hybrid DFTB/MM-based method for materials science[41] and the combination of the recently developed partial charge MM potential[87] with current parameters allow one to investigate much larger systems with a near-realistic timescale using considerably less computational effort compared to the case with full-QM methods. We argue that the currently developed parameters provide adequate and reliable semiquantitative agreement with respect to both reference DFT and experimental data. Thus, the currently developed parameters should serve as an excellent tool for future investigations of processes on oxide surfaces, in particular on the monoclinic ZrO_2, tetragonal ZrO_2, cubic Y_2O_3, and tetragonal YSZ surfaces. Currently, the parameters are extended to include interactions between the metals and carbon, hydrogen, nitrogen, phosphorous, and sulfur, which will be reported elsewhere.

From the development perspective, a more sophisticated and robust DFTB repulsive potential fitting can be employed to overcome the limited transferability of the 2-body repulsive potential required in the case of more complex structures. Approaches beyond the applications of a 2-body repulsive potential, including the recently developed many-body repulsive potential based on a deep tensor neural network by Stöhr *et al.*[113] and curvature constrained splines by Kandy *et al.*,[114] represent key steps toward this goal. Although the inclusion of the latter innovations proved to be beyond the scope of the present work, the applicability of such methods is possibly explored in the near future. Thus, the present parameterization also represents a primer for the development of an improved DFTB parameterization aimed at the treatment of more complex chemical systems.

■ ASSOCIATED CONTENT

Supporting Information

The Supporting Information is available free of charge at https://pubs.acs.org/doi/10.1021/acsomega.1c02411.

RDFs of YSZ*n* (n = 4 and 12), geometries of *t*-ZrO_2 (101) and *c*-Y_2O_3 (110) surfaces at 298.15 K, example of unsuitable parameterizations, and fractional coordinates of the atoms in *c*-Y_2O_3 (PDF)

SK files used in this work (ZIP)

■ AUTHOR INFORMATION

Corresponding Author

Aulia Sukma Hutama − *Department of Chemistry, Faculty of Mathematics and Natural Sciences, Universitas Gadjah Mada, Yogyakarta 55281, Indonesia;* orcid.org/0000-0002-3322-9421; Email: aulia.sukma.hutama@ugm.ac.id

https://doi.org/10.1021/acsomega.1c02411
ACS Omega 2021, 6, 20530−20548

Authors

Lala Adetia Marlina − *Department of Chemistry, Faculty of Mathematics and Natural Sciences, Universitas Gadjah Mada, Yogyakarta 55281, Indonesia*

Chien-Pin Chou − *Department of Applied Chemistry, National Chiao Tung University, Hsinchu 30010, Taiwan;* Present Address: JSR Corporation, 100 Kawajiri-cho, Yokkaichi, Mie 510-8552, Japan

Stephan Irle − *Computational Sciences and Engineering Division & Chemical Sciences Division, Oak Ridge National Laboratory, Oak Ridge, Tennessee 37830, United States;* orcid.org/0000-0003-4995-4991

Thomas S. Hofer − *Theoretical Chemistry Division, Institute of General, Inorganic and Theoretical Chemistry, Center for Chemistry and Biomedicine, University of Innsbruck, Innsbruck A-6020, Austria*

Complete contact information is available at: https://pubs.acs.org/10.1021/acsomega.1c02411

Notes

The authors declare no competing financial interest.

■ ACKNOWLEDGMENTS

The research reported in this publication was jointly supported by the ASEAN-European Academic University Network (ASEA-UNINET) and the Austrian Agency for International Cooperation in Education and Research (OeAD-GmbH). A.S.H. acknowledges support from the Faculty of Mathematics and Natural Sciences, Universitas Gadjah Mada under the contract number 183/J01.1.28/PL.06.02/2021. S.I. acknowledges support from the U.S. Department of Energy, Office of Science, Office of Basic Energy Sciences, Chemical Sciences, Geosciences, and Biosciences Division, Catalysis Science Program.

■ REFERENCES

(1) Cao, X. Q.; Vassen, R.; Stoever, D. Ceramic materials for thermal barrier coatings. *J. Eur. Ceram. Soc.* **2004**, *24*, 1−10.

(2) Li, H.; Rameshan, C.; Bukhtiyarov, A. V.; Prosvirin, I. P.; Bukhtiyarov, V. I.; Rupprechter, G. CO_2 activation on ultrathin ZrO_2 film by H_2O co-adsorption: In situ NAP-XPS and IRAS studies. *Surf. Sci.* **2019**, *679*, 139−146.

(3) Zhang, Y.; Chen, C.; Lin, X.; Li, D.; Chen, X.; Zhan, Y.; Zheng, Q. CuO/ZrO_2 catalysts for water-gas shift reaction: Nature of catalytically active copper species. *Int. J. Hydrogen Energy* **2014**, *39*, 3746−3754.

(4) Yan, G. X.; Wang, A.; Wachs, I. E.; Baltrusaitis, J. Critical review on the active site structure of sulfated zirconia catalysts and prospects in fuel production. *Appl. Catal., A* **2019**, *572*, 210−225.

(5) Wang, P.; Yue, Y.; Wang, T.; Bao, X. Alkane isomerization over sulfated zirconia solid acid system. *Int. J. Energy Res.* **2020**, *44*, 3270−3294.

(6) Abriata, J. P.; Garcés, J.; Versaci, R. The O-Zr (Oxygen-Zirconium) system. *Bull. Alloy Phase Diagrams* **1986**, *7*, 116−124.

(7) Singh, A. P.; Kaur, N.; Kumar, A.; Singh, K. L. Preparation of fully cubic calcium-stabilized zirconia with 10 mol% calcium oxide dopant concentration by microwave processing. *J. Am. Ceram. Soc.* **2007**, *90*, 789−796.

(8) Keerthana, L.; Sakthivel, C.; Prabha, I. $MgO-ZrO_2$ mixed nanocomposites: fabrication methods and applications. *Mater. Today Sustain.* **2019**, *3*−*4*, 100007.

(9) Lashtabeg, A.; Skinner, S. J. Solid oxide fuel cells-a challenge for materials chemists? *J. Mater. Chem.* **2006**, *16*, 3161−3170.

(10) Malavasi, L.; Fisher, C. A. J.; Islam, M. S. Oxide-ion and proton conducting electrolyte materials for clean energy applications: structural and mechanistic features. *Chem. Soc. Rev.* **2010**, *39*, 4370−4387.

(11) Gómez, S. Y.; Hotza, D. Current developments in reversible solid oxide fuel cells. *Renewable Sustainable Energy Rev.* **2016**, *61*, 155−174.

(12) Miura, N.; Sato, T.; Anggraini, S. A.; Ikeda, H.; Zhuiykov, S. A review of mixed-potential type zirconia-based gas sensors. *Ionics* **2014**, *20*, 901−925.

(13) Liu, T.; Zhang, X.; Yuan, L.; Yu, J. A review of high-temperature electrochemical sensors based on stabilized zirconia. *Solid State Ionics* **2015**, *283*, 91−102.

(14) Tsampas, M. N.; Sapountzi, F. M.; Vernoux, P. Applications of yttria stabilized zirconia (YSZ) in catalysis. *Catal. Sci. Technol.* **2015**, *5*, 4884−4900.

(15) Brinkman, H. W.; Briels, W. J.; Verweij, H. Molecular dynamics simulations of yttria-stabilized zirconia. *Chem. Phys. Lett.* **1995**, *247*, 386−390.

(16) Schelling, P. K.; Phillpot, S. R.; Wolf, D. Mechanism of the cubic-to-tetragonal phase transition in zirconia and yttria-stabilized zirconia by molecular-dynamics simulation. *J. Am. Ceram. Soc.* **2001**, *84*, 1609−1619.

(17) Kilo, M.; Argirusis, C.; Borchardt, G.; Jackson, R. A. Oxygen diffusion in yttria stabilised zirconia - Experimental results and molecular dynamics calculations. *Phys. Chem. Chem. Phys.* **2003**, *5*, 2219−2224.

(18) Van Duin, A. C. T.; Merinov, B. V.; Jang, S. S.; Goddard, W. A. ReaxFF reactive force field for solid oxide fuel cell systems with application to oxygen ion transport in yttria-stabilized zirconia. *J. Phys. Chem. A* **2008**, *112*, 3133−3140.

(19) Mayernick, A. D.; Batzill, M.; van Duin, A. C. T.; Janik, M. J. A reactive force-field (ReaxFF) Monte Carlo study of surface enrichment and step structure on yttria-stabilized zirconia. *Surf. Sci.* **2010**, *604*, 1438−1444.

(20) Lau, K. C.; Dunlap, B. I. Molecular dynamics simulation of yttria-stabilized zirconia (YSZ) crystalline and amorphous solids. *J. Phys.: Condens. Matter* **2011**, *23*, 035401.

(21) Huang, H. C.; Su, P.-C.; Kwak, S. K.; Pornprasertsuk, R.; Yoon, Y.-J. Molecular dynamics simulation of oxygen ion diffusion in yttria stabilized zirconia single crystals and bicrystals. *Fuel Cells* **2014**, *14*, 574−580.

(22) Sizov, V. V.; Lampinen, M. J.; Laaksonen, A. Molecular dynamics simulation of oxygen diffusion in cubic yttria-stabilized zirconia: Effects of temperature and composition. *Solid State Ionics* **2014**, *266*, 29−35.

(23) González-Romero, R. L.; Meléndez, J. J. Yttrium segregation and oxygen diffusion along high-symmetry grain boundaries in YSZ. *J. Alloys Compd.* **2015**, *622*, 708−713.

(24) Tarancón, A.; Morata, A. New insights into the origin of the oxide ionic diffusion change in strained lattices of yttria stabilized zirconia. *Comput. Mater. Sci.* **2015**, *103*, 206−215.

(25) Iskandarov, A. M.; Umeno, Y. Atomistic modeling study of surface effect on oxide ion diffusion in yttria-stabilized zirconia. *Solid State Ionics* **2015**, *279*, 46−52.

(26) Houska, J. Force field for realistic molecular dynamics simulations of ZrO_2 growth. *Comput. Mater. Sci.* **2016**, *111*, 209−217.

(27) Lu, Z.; Chernatynskiy, A.; Noordhoek, M. J.; Sinnott, S. B.; Phillpot, S. R. Nanoindentation of ZrO_2 and ZrO_2/Zr systems by molecular dynamics simulation. *J. Nucl. Mater.* **2017**, *486*, 250−266.

(28) Wang, X.; Huang, W.; Zhu, C.; Chen, Q.; Pilla, S.; Liang, G. Porosity effects on oxygen ions diffusion in the yttria-stabilized zirconia (YSZ) by molecular dynamics simulation. *J. Mol. Liq.* **2018**, *265*, 31−35.

(29) Jaipal, M.; Chatterjee, A. Effect of the $\Sigma5(310)/[001]$ tilt grain boundary on oxygen-ion movement in yttria-stabilized zirconia: Insights from molecular dynamics. *Acta Mater.* **2019**, *165*, 307−314.

(30) Deng, B.; Luo, J.; Harris, J. T.; Smith, C. M. Critical stress map for ZrO_2 tetragonal to monoclinic phase transformation in ZrO_2-toughened glass-ceramics. *Materialia* **2020**, *9*, 100548.

(31) Wang, X.; Pilla, S.; Che, J.; Chen, Q. Porous effects on heat transfer and ions distribution in YSZ using molecular dynamics simulation. *Chem. Phys. Lett.* **2020**, *747*, 137339.
(32) Zhou, J.; Zhang, J.; Zhong, Z. Mechanical properties of yttria-stabilized zirconia: A study by ReaxFF molecular dynamics simulations. *Mech. Mater.* **2020**, *149*, 103542.
(33) Porezag, D.; Frauenheim, T.; Köhler, T.; Seifert, G.; Kaschner, R. Construction of tight-binding-like potentials on the basis of density-functional theory: Application to carbon. *Phys. Rev. B: Condens. Matter Mater. Phys.* **1995**, *51*, 12947−12957.
(34) Elstner, M.; Porezag, D.; Jungnickel, G.; Elsner, J.; Haugk, M.; Frauenheim, T.; Suhai, S.; Seifert, G. Self-consistent-charge density-functional tight-binding method for simulations of complex materials properties. *Phys. Rev. B: Condens. Matter Mater. Phys.* **1998**, *58*, 7260−7268.
(35) Köhler, C.; Seifert, G.; Gerstmann, U.; Elstner, M.; Overhof, H.; Frauenheim, T. Approximate density-functional calculations of spin densities in large molecular systems and complex solids. *Phys. Chem. Chem. Phys.* **2001**, *3*, 5109−5114.
(36) Köhler, C.; Seifert, G.; Frauenheim, T. Density functional based calculations for Fe_n ($n \leq 32$). *Chem. Phys.* **2005**, *309*, 23−31.
(37) Niehaus, T. A.; Suhai, S.; Della Sala, F.; Elstner, M.; Seifert, G.; Frauenheim, T. Tight-binding approach to time-dependent density-functional response theory. *Phys. Rev. B: Condens. Matter Mater. Phys.* **2001**, *63*, 085108.
(38) Domínguez, A.; Aradi, B.; Frauenheim, T.; Lutsker, V.; Niehaus, T. A. Extensions of the time-dependent density functional based tight-binding approach. *J. Chem. Theory Comput.* **2013**, *9*, 4901−4914.
(39) Paris, A.; Taioli, S. Multiscale investigation of oxygen vacancies in TiO_2 anatase and their role in memristor's behavior. *J. Phys. Chem. C* **2016**, *120*, 22045−22053.
(40) Page, A. J.; Wang, Y.; Li, H.-B.; Irle, S.; Morokuma, K. Nucleation of graphene precursors on transition metal surfaces: Insights from theoretical simulations. *J. Phys. Chem. C* **2013**, *117*, 14858−14864.
(41) Saleh, M.; Hofer, T. S. A DFTB/MM MD approach for solid-state interfaces: Structural and dynamical properties of H_2O and NH_3 on R-TiO_2 (001). *J. Phys. Chem. C* **2019**, *123*, 7230−7245.
(42) Koskinen, P.; Mäkinen, V. Density-functional tight-binding for beginners. *Comput. Mater. Sci.* **2009**, *47*, 237−253.
(43) Hourahine, B.; Aradi, B.; Blum, V.; Bonafé, F.; Buccheri, A.; Camacho, C.; Cevallos, C.; Deshaye, M. Y.; Dumitrică, T.; Dominguez, A.; et al. DFTB+, a software package for efficient approximate density functional theory based atomistic simulations. *J. Chem. Phys.* **2020**, *152*, 124101.
(44) Witek, H. A.; Köhler, C.; Frauenheim, T.; Morokuma, K.; Elstner, M. Relativistic parametrization of the self-consistent-charge density-functional tight-binding method. 1. Atomic wave functions and energies. *J. Phys. Chem. A* **2007**, *111*, 5712−5719.
(45) Nishimura, Y. Development of the density functional tight binding method and its application in computational nanomaterial science. Ph.D. Thesis; Nagoya University, 2013.
(46) Hutama, A. S.; Chou, C.-P.; Nishimura, Y.; Witek, H. A.; Irle, S. Density-functional tight-binding parameters for bulk zirconium: A case study for repulsive potentials. *J. Phys. Chem. A* **2021**, *125*, 2184−2196.
(47) Hellström, M.; Jorner, K.; Bryngelsson, M.; Huber, S. E.; Kullgren, J.; Frauenheim, T.; Broqvist, P. An SCC-DFTB repulsive potential for various ZnO polymorphs and the ZnO−water system. *J. Phys. Chem. C* **2013**, *117*, 17004−17015.
(48) Moreira, N. H.; Dolgonos, G.; Aradi, B.; da Rosa, A. L.; Frauenheim, T. Toward an accurate density-functional tight-binding description of Zinc-containing compounds. *J. Chem. Theory Comput.* **2009**, *5*, 605−614.
(49) Bodrog, Z.; Aradi, B.; Frauenheim, T. Automated repulsive parametrization for the DFTB method. *J. Chem. Theory Comput.* **2011**, *7*, 2654−2664.
(50) Zinkevich, M. Thermodynamics of rare earth sesquioxides. *Prog. Mater. Sci.* **2007**, *52*, 597−647.
(51) Perdew, J. P.; Burke, K.; Ernzerhof, M. Generalized gradient approximation made simple. *Phys. Rev. Lett.* **1996**, *77*, 3865−3868.
(52) Blöchl, P. E. Projector augmented-wave method. *Phys. Rev. B: Condens. Matter Mater. Phys.* **1994**, *50*, 17953−17979.
(53) Kresse, G.; Hafner, J. Ab initio molecular dynamics for liquid metals. *Phys. Rev. B: Condens. Matter Mater. Phys.* **1993**, *47*, 558−561.
(54) Kresse, G.; Hafner, J. Ab initio molecular-dynamics simulation of the liquid-metal−amorphous-semiconductor transition in germanium. *Phys. Rev. B: Condens. Matter Mater. Phys.* **1994**, *49*, 14251−14269.
(55) Kresse, G.; Furthmüller, J. Efficient iterative schemes for ab initio total-energy calculations using a plane-wave basis set. *Phys. Rev. B: Condens. Matter Mater. Phys.* **1996**, *54*, 11169−11186.
(56) Kresse, G.; Furthmüller, J. Efficiency of ab-initio total energy calculations for metals and semiconductors using a plane-wave basis set. *Comput. Mater. Sci.* **1996**, *6*, 15−50.
(57) Aradi, B.; Hourahine, B.; Frauenheim, T. DFTB+, a sparse matrix-based implementation of the DFTB method. *J. Phys. Chem. A* **2007**, *111*, 5678−5684.
(58) Togo, A.; Tanaka, I. First principles phonon calculations in materials science. *Scr. Mater.* **2015**, *108*, 1−5.
(59) Witek, H. A.; Chou, C. P.; Mazur, G.; Nishimura, Y.; Irle, S.; Aradi, B.; Frauenheim, T.; Morokuma, K. Automatized parameterization of the density-functional tight-binding method. II. Two-center integrals. *J. Chin. Chem. Soc.* **2015**, *63*, 57−68.
(60) Chou, C.-P.; Nishimura, Y.; Fan, C.-C.; Mazur, G.; Irle, S.; Witek, H. A. Automatized parameterization of DFTB using particle swarm optimization. *J. Chem. Theory Comput.* **2016**, *12*, 53−64.
(61) Chou, C.-P. Automatic Density Functional Tight Binding Parameterization Toolkit. https://bitbucket.org/solccp/adpt_core/ (accessed 20 09 2020)
(62) Berendsen, H. J. C.; Grigera, J. R.; Straatsma, T. P. The missing term in effective pair potentials. *J. Phys. Chem.* **1987**, *91*, 6269−6271.
(63) Perdew, J. P.; Ruzsinszky, A.; Csonka, G. I.; Vydrov, O. A.; Scuseria, G. E.; Constantin, L. A.; Zhou, X.; Burke, K. Restoring the density-gradient expansion for exchange in solids and surfaces. *Phys. Rev. Lett.* **2008**, *100*, 136406.
(64) Dovesi, R.; Erba, A.; Orlando, R.; Zicovich-Wilson, C. M.; Civalleri, B.; Maschio, L.; Rérat, M.; Casassa, S.; Baima, J.; Salustro, S.; et al. Quantum-mechanical condensed matter simulations with CRYSTAL. *WIREs Comp. Mol. Sci.* **2018**, *8*, No. e1360.
(65) Houssa, M.; Afanas'ev, V. V.; Stesmans, A.; Heyns, M. M. Variation in the fixed charge density of SiO_x/ZrO_2 gate dielectric stacks during postdeposition oxidation. *Appl. Phys. Lett.* **2000**, *77*, 1885−1887.
(66) Sayan, S.; Bartynski, R. A.; Zhao, X.; Gusev, E. P.; Vanderbilt, D.; Croft, M.; Banaszak Holl, M.; Garfunkel, E. Valence and conduction band offsets of a ZrO_2/SiO_xN_y/n-Si CMOS gate stack: A combined photoemission and inverse photoemission study. *Phys. Status Solidi B* **2004**, *241*, 2246−2252.
(67) Atabaev, T. S.; Hwang, Y.-H.; Kim, H.-K. Color-tunable properties of Eu^{3+}- and Dy^{3+}-codoped Y_2O_3 phosphor particles. *Nanoscale Res. Lett.* **2012**, *7*, 556.
(68) Hourahine, B.; Sanna, S.; Aradi, B.; Köhler, C.; Niehaus, T.; Frauenheim, T. Self-interaction and strong correlation in DFTB. *J. Phys. Chem. A* **2007**, *111*, 5671−5677.
(69) Niehaus, T. A.; Sala, F. D. Range separated functionals in the density functional based tight-binding method: Formalism. *Phys. Status Solidi B* **2012**, *249*, 237−244.
(70) Lutsker, V.; Aradi, B.; Niehaus, T. A. Implementation and benchmark of a long-range corrected functional in the density functional based tight-binding method. *J. Chem. Phys.* **2015**, *143*, 184107.
(71) Koch, D.; Manzhos, S. On the charge state of titanium in titanium dioxide. *J. Phys. Chem. Lett.* **2017**, *8*, 1593−1598.

https://doi.org/10.1021/acsomega.1c02411
ACS Omega 2021, 6, 20530−20548

(72) Zandiehnadem, F.; Murray, R. A.; Ching, W. Y. Electronic structures of three phases of zirconium oxide. *Phys. B+C* **1988**, *150*, 19−24.
(73) Christensen, A.; Carter, E. A. First-principles characterization of a heteroceramic interface: ZrO_2 deposited on an α-Al_2O_3 (1102) substrate. *Phys. Rev. B: Condens. Matter Mater. Phys.* **2000**, *62*, 16968−16983.
(74) Wang, B.; Li, S. L.; Truhlar, D. G. Modeling the partial atomic charges in inorganometallic molecules and solids and charge redistribution in lithium-ion cathodes. *J. Chem. Theory Comput.* **2014**, *10*, 5640−5650.
(75) Birch, F. Finite elastic strain of cubic crystals. *Phys. Rev.* **1947**, *71*, 809−824.
(76) Hutama, A. S.; Nishimura, Y.; Chou, C.-P.; Irle, S. Development of density-functional tight-binding repulsive potentials for bulk zirconia using particle swarm optimization algorithm. *AIP Conf. Proc.* **2017**, *1906*, 030015.
(77) Kuwabara, A.; Tohei, T.; Yamamoto, T.; Tanaka, I. Ab initio lattice dynamics and phase transformations of ZrO_2. *Phys. Rev. B: Condens. Matter Mater. Phys.* **2005**, *71*, 064301.
(78) Franke, D.; Hettich, C.; Köhler, T.; Turowski, M.; Ehlers, H.; Ristau, D.; Frauenheim, T. Density functional based tight-binding parametrization of hafnium oxide: Simulations of amorphous structures. *Phys. Rev. B* **2018**, *98*, 075207.
(79) Lee, J.; Ganguli, S.; Roy, A. K.; Badescu, S. C. Density functional tight binding study of β-Ga_2O_3: Electronic structure, surface energy, and native point defects. *J. Chem. Phys.* **2019**, *150*, 174706.
(80) Liu, B.; Xiao, H.; Zhang, Y.; Aidhy, D. S.; Weber, W. J. Investigation of oxygen point defects in cubic ZrO_2 by density functional theory. *Comput. Mater. Sci.* **2014**, *92*, 22−27.
(81) Youssef, M.; Yildiz, B. Intrinsic point-defect equilibria in tetragonal ZrO_2: Density functional theory analysis with finite-temperature effects. *Phys. Rev. B: Condens. Matter Mater. Phys.* **2012**, *86*, 144109.
(82) Ran, S.; Winnubst, L.; Wiratha, W.; Blank, D. H. Sintering behavior of 0.8 mol%-CuO-doped 3Y-TZP ceramics. *J. Am. Ceram. Soc.* **2006**, *89*, 151−155.
(83) Teufer, G. The crystal structure of tetragonal ZrO_2. *Acta Crystallogr.* **1962**, *15*, 1187.
(84) Bai, X.-M.; Zhang, Y.; Tonks, M. R. Strain effects on oxygen transport in tetragonal zirconium dioxide. *Phys. Chem. Chem. Phys.* **2013**, *15*, 19438−19449.
(85) Pecharromán, C.; Ocaña, M.; Serna, C. J. Optical constants of tetragonal and cubic zirconias in the infrared. *J. Appl. Phys.* **1996**, *80*, 3479−3483.
(86) Rignanese, G.-M.; Detraux, F.; Gonze, X.; Pasquarello, A. First-principles study of dynamical and dielectric properties of tetragonal zirconia. *Phys. Rev. B: Condens. Matter Mater. Phys.* **2001**, *64*, 134301.
(87) Hofer, T. S.; Kilchert, F. M.; Tanjung, B. A. An effective partial charge model for bulk and surface properties of cubic ZrO_2, Y_2O_3 and yttrium-stabilised zirconia. *Phys. Chem. Chem. Phys.* **2019**, *21*, 25635−25648.
(88) Ferreira, F. F.; Granado, E.; Carvalho Jr, W.; Kycia, S. W.; Bruno, D.; Droppa Jr, R. X-ray powder diffraction beamline at D10B of LNLS: Application to the Ba_2FeReO_6 double perovskite. *J. Synchrotron Radiat.* **2006**, *13*, 46−53.
(89) Kruk, A.; Wajler, A.; Bobruk, M.; Adamczyk, A.; Mrózek, M.; Gawlik, W.; Brylewski, T. Preparation of yttria powders co-doped with Nd^{3+}, and La^{3+} using EDTA gel processes for application in transparent ceramics. *J. Eur. Ceram. Soc.* **2017**, *37*, 4129−4140.
(90) Gibson, I. R.; Dransfield, G. P.; Irvine, J. T. Sinterability of commercial 8 mol% yttria-stabilized zirconia powders and the effect of sintered density on the ionic conductivity. *J. Mater. Sci.* **1998**, *33*, 4297−4305.
(91) Suciu, C.; Dorolti, E.; Hoffmann, A. C. Physico-chemical properties of nanocrystalline YSZ powders as a function of doping level and electrical properties after sintering. *Mater. Sci. Energy Technol.* **2018**, *1*, 136−145.
(92) Kawata, K.; Maekawa, H.; Nemoto, T.; Yamamura, T. Local structure analysis of YSZ by Y-89 MAS-NMR. *Solid State Ionics* **2006**, *177*, 1687−1690.
(93) Morterra, C.; Cerrato, G.; Ferroni, L.; Montanaro, L. Surface characterization of yttria-stabilized tetragonal ZrO_2 Part 1. Structural, morphological, and surface hydration features. *Mater. Chem. Phys.* **1994**, *37*, 243−257.
(94) Orlando, R.; Pisani, C.; Roetti, C.; Stefanovich, E. Ab initio Hartree-Fock study of tetragonal and cubic phases of zirconium dioxide. *Phys. Rev. B: Condens. Matter Mater. Phys.* **1992**, *45*, 592−601.
(95) Christensen, A.; Carter, E. A. First-principles study of the surfaces of zirconia. *Phys. Rev. B: Condens. Matter Mater. Phys.* **1998**, *58*, 8050−8064.
(96) Eichler, A.; Kresse, G. First-principles calculations for the surface termination of pure and yttria-doped zirconia surfaces. *Phys. Rev. B: Condens. Matter Mater. Phys.* **2004**, *69*, 045402.
(97) Ricca, C.; Ringuedé, A.; Cassir, M.; Adamo, C.; Labat, F. A comprehensive DFT investigation of bulk and low-index surfaces of ZrO_2 polymorphs. *J. Comput. Chem.* **2015**, *36*, 9−21.
(98) Hofmann, A.; Clark, S. J.; Oppel, M.; Hahndorf, I. Hydrogen adsorption on the tetragonal ZrO_2(101) surface: A theoretical study of an important catalytic reactant†. *Phys. Chem. Chem. Phys.* **2002**, *4*, 3500−3508.
(99) Añez, R.; Sierraalta, A.; Martorell, G.; Sautet, P. Stabilization of the (1 1 0) tetragonal zirconia surface by hydroxyl chemical transformation. *Surf. Sci.* **2009**, *603*, 2526−2531.
(100) Sato, R.; Ohkuma, S.; Shibuta, Y.; Shimojo, F.; Yamaguchi, S. Proton migration on hydrated surface of cubic ZrO_2: ab initio molecular dynamics simulation. *J. Phys. Chem. C* **2015**, *119*, 28925−28933.
(101) Cadi-Essadek, A.; Roldan, A.; de Leeuw, N. H. Density functional theory study of the interaction of H_2O, CO_2 and CO with the ZrO_2 (111), Ni/ZrO_2 (111), YSZ (111) and Ni/YSZ (111) surfaces. *Surf. Sci.* **2016**, *653*, 153−162.
(102) Hofmann, A.; Sauer, J. Surface structure of hydroxylated and sulfated zirconia. A periodic density-functional study. *J. Phys. Chem. B* **2004**, *108*, 14652−14662.
(103) Dolgonos, G.; Aradi, B.; Moreira, N. H.; Frauenheim, T. An improved self-consistent-charge density-functional tight-binding (SCC-DFTB) set of parameters for simulation of bulk and molecular systems involving titanium. *J. Chem. Theory Comput.* **2010**, *6*, 266−278.
(104) Luo, X.; Zhou, W.; Ushakov, S. V.; Navrotsky, A.; Demkov, A. A. Monoclinic to tetragonal transformations in hafnia and zirconia: A combined calorimetric and density functional study. *Phys. Rev. B: Condens. Matter Mater. Phys.* **2009**, *80*, 134119.
(105) Gennard, S.; Corà, F.; Catlow, C. R. A.; Catlow, A. Comparison of the bulk and surface properties of ceria and zirconia by ab initio investigations. *J. Phys. Chem. B* **1999**, *103*, 10158−10170.
(106) Köck, E.-M.; Kogler, M.; Bielz, T.; Klötzer, B.; Penner, S. In situ FT-IR spectroscopic study of CO_2 and CO adsorption on Y_2O_3, ZrO_2, and yttria-stabilized ZrO_2. *J. Phys. Chem. C* **2013**, *117*, 17666−17673.
(107) Kogler, M.; Köck, E.-M.; Perfler, L.; Bielz, T.; Stöger-Pollach, M.; Hetaba, W.; Willinger, M.; Huang, X.; Schuster, M.; Klötzer, B.; et al. Methane decomposition and carbon growth on Y_2O_3, yttria-stabilized zirconia, and ZrO_2. *Chem. Mater.* **2014**, *26*, 1690−1701.
(108) Kogler, M.; Köck, E.-M.; Bielz, T.; Pfaller, K.; Klötzer, B.; Schmidmair, D.; Perfler, L.; Penner, S. Hydrogen surface reactions and adsorption studied on Y_2O_3, YSZ, and ZrO_2. *J. Phys. Chem. C* **2014**, *118*, 8435−8444.
(109) Kogler, M.; Köck, E.-M.; Klötzer, B.; Perfler, L.; Penner, S. Surface reactivity of YSZ, Y_2O_3, and ZrO_2 toward CO, CO_2, and CH_4: A comparative discussion. *J. Phys. Chem. C* **2016**, *120*, 3882−3898.
(110) Köck, E.-M.; Kogler, M.; Klötzer, B.; Noisternig, M. F.; Penner, S. Structural and electrochemical properties of physisorbed and chemisorbed water layers on the ceramic oxides Y_2O_3, YSZ, and ZrO_2. *ACS Appl. Mater. Interfaces* **2016**, *8*, 16428−16443.

https://doi.org/10.1021/acsomega.1c02411
ACS Omega 2021, 6, 20530−20548

(111) Zhu, J.; Zhu, Y.; Shen, W.; Wang, Y.; Han, J.; Tian, G.; Lei, P.; Dai, B. Growth and characterization of yttrium oxide films by reactive magnetron sputtering. *Thin Solid Films* **2011**, *519*, 4894−4898.
(112) Dimoulas, A.; Travlos, A.; Vellianitis, G.; Boukos, N.; Argyropoulos, K. Direct heteroepitaxy of crystalline Y_2O_3 on Si (001) for high-k gate dielectric applications. *J. Appl. Phys.* **2001**, *90*, 4224−4230.
(113) Stöhr, M.; Medrano Sandonas, L.; Tkatchenko, A. Accurate many-body repulsive potentials for density-functional tight binding from deep tensor neural networks. *J. Phys. Chem. Lett.* **2020**, *11*, 6835−6843.
(114) Kandy, A. K. A.; Wadbro, E.; Aradi, B.; Broqvist, P.; Kullgren, J. Curvature constrained splines for DFTB repulsive potential parametrization. *J. Chem. Theory Comput.* **2021**, *17*, 1771−1781.
(115) Hao, Y.-J.; Zhang, L.; Chen, X.-R.; Li, Y.-H.; He, H.-L. Phase transition and elastic constants of zirconium from first-principles calculations. *J. Phys.: Condens. Matter* **2008**, *20*, 235230.
(116) Zhao, Y.; Zhang, J.; Pantea, C.; Qian, J.; Daemen, L. L.; Rigg, P. A.; Hixson, R. S.; Gray, G. T.; Yang, Y.; Wang, L.; et al. Thermal equations of state of the α, β, and ω phases of zirconium. *Phys. Rev. B: Condens. Matter Mater. Phys.* **2005**, *71*, 184119.
(117) Spedding, F. H.; Daane, A. H.; Herrmann, K. W. The crystal structures and lattice parameters of high-purity scandium, yttrium and the rare earth metals. *Acta Crystallogr.* **1956**, *9*, 559−563.
(118) Smith, D. K.; Newkirk, W. The crystal structure of baddeleyite (monoclinic ZrO_2) and its relation to the polymorphism of ZrO_2. *Acta Crystallogr.* **1965**, *18*, 983−991.
(119) Leger, J. M.; Tomaszewski, P. E.; Atouf, A.; Pereira, A. S. Pressure-induced structural phase transitions in zirconia under high pressure. *Phys. Rev. B: Condens. Matter Mater. Phys.* **1993**, *47*, 14075−14083.
(120) Mashimo, T.; Nagayama, K.; Sawaoka, A. Shock compression of zirconia ZrO_2 and zircon $ZrSiO_4$ in the pressure range up to 150 GPa. *Phys. Chem. Miner.* **1983**, *9*, 237−247.
(121) Kisi, E. H.; Howard, C. J. Crystal Structures of zirconia phases and their inter-relation. *Key Eng. Mater.* **1998**, *153*−*154*, 1−36.
(122) Coughlin, J. P.; King, E. G. High-temperature heat contents of some zirconium-containing substances. *J. Am. Chem. Soc.* **1950**, *72*, 2262−2265.
(123) Yashima, M.; Mitsuhashi, T.; Takashina, H.; Kakihana, M.; Ikegami, T.; Yoshimura, M. Tetragonal-monoclinic phase transition enthalpy and temperature of ZrO_2-CeO_2 solid solutions. *J. Am. Ceram. Soc.* **1995**, *78*, 2225−2228.
(124) Suresh, A.; Porter, W. D.; Mayo, M. J.; Porter, W. D. Thermodynamics of the tetragonal-to-monoclinic phase transformation in fine and nanocrystalline yttria-stabilized zirconia powders. *J. Mater. Res.* **2003**, *18*, 2912−2921.
(125) Yeheskel, O.; Tevet, O. Elastic moduli of transparent yttria. *J. Am. Ceram. Soc.* **1999**, *82*, 136−144.

https://doi.org/10.1021/acsomega.1c02411
ACS Omega 2021, 6, 20530−20548